Spring 5-8-2020

Characterization of Photoacoustic Flow Cytometry Signals

Craig Benzinger

CHARACTERIZATION OF PHOTOACOUSTIC FLOW CYTOMETRY DETECTION SIGNALS

A Thesis

Submitted to the Rangos School of Health Sciences

Duquesne University

In partial fulfillment of the requirements for

the degree of Master of Biomedical Engineering

By

Craig Benzinger Jr.

May 2020

CHARACTERIZATION OF PHOTOACOUSTIC

FLOW CYTOMETRY DETECTION SIGNALS

By

Craig Benzinger Jr.

Approved April 6, 2020

_____	_____
John A. Viator, Ph.D. Professor of Biomedical Engineering (Committee Chair)	Rana Zakerzadeh, Ph.D. Assistant Professor of Biomedical Engineering (Committee Member)
_____	_____
Fevzi Akinci, Ph.D. Dean, Rangos School of Health Sciences Professor of Health Administration	John A. Viator, Ph.D. Chair, Biomedical Engineering Professor of Biomedical Engineering

ABSTRACT

CHARACTERIZATION OF PHOTOACOUSTIC FLOW CYTOMETRY DETECTION SIGNALS

By

Craig Benzinger Jr.

May 2020

Dissertation supervised by Dr. John Viator

Photoacoustic flow cytometry has been utilized to clinically determine the presence of melanoma circulating tumor cells (CTCs). Further investigation was conducted into the morphology of detection signals and how they could be manipulated to allow for further classification. Novel features were extracted from waveforms that appear to have strong classification ability. Neural networks were also used to determine classification potential and the creation of feature mapping for future unsupervised classification. Detections were expanded from single waves to a time dependent multi-wave event. Waveforms were also determined to be of non-parametric distribution, allowing for classification by neural network but not allowing for reduction into feature maps with techniques used in the study.

DEDICATION

To my family.

TABLE OF CONTENTS

Page

Introduction

Objective

Previously, is has been demonstrated that photoacoustic flow cytometry is an effective method for detection of circulating melanoma tumor cells. By exciting the cells contained in a patient's liquid biopsy using laser energy, acoustic signals characteristic to melanoma would breech preset thresholds determining cell presence. This would allow for detection and subsequent enumeration of tumor cells present in the biopsy. Melanoma cells are able to be detected without prior staining due to the inherit pigment contained within the cells. It will be demonstrated in this research that the accuracy of this method can be improved through more sophisticated data analysis techniques. By expanding the amount of data analyzed and employing multiple machine learning techniques, detection of melanoma CTCs can be accomplished with higher accuracy than previous methods. To summarize the objective of this work, an investigation was devised to determine the ability to classify photoacoustic signals from cancel cells. This investigation leveraged both neural network and fundamental analysis techniques.

Circulating Tumor Cells

Circulating tumor cells (CTCs) are often symptomatic of a stage IV cancer diagnosis. Multiple cancers have been tested including colorectal, pancreatic, and lung cancer. In all studies it was determined that CTCs were an efficient tool for a stage IV cancer prognosis[1,2,3]. CTCs occur when the cancerous growth has advanced into the vascular or lymph system. Often the cancer will degrade when in contact with these fluid systems and cell particulates will detach from the main tumor.

In this event cancerous cells will spread throughout the body using the vasculature resulting in metastasis, the growth of additional tumors (Fig. 1). CTCs are a highly studied area and are hypothesized to be a great predictor of relapse from remission[4]. The fact stands that any person who has developed cancer will have CTCs in their fluid systems regardless of remission status[5,6]. During chemotherapy treatments, CTCs will also be measured to assess the effectiveness of the treatment[7,8,9]. At this point there has been no significant evidence that switching treatments due to increase or stagnant levels of CTCs post treatment has led to an increase in remission[10].

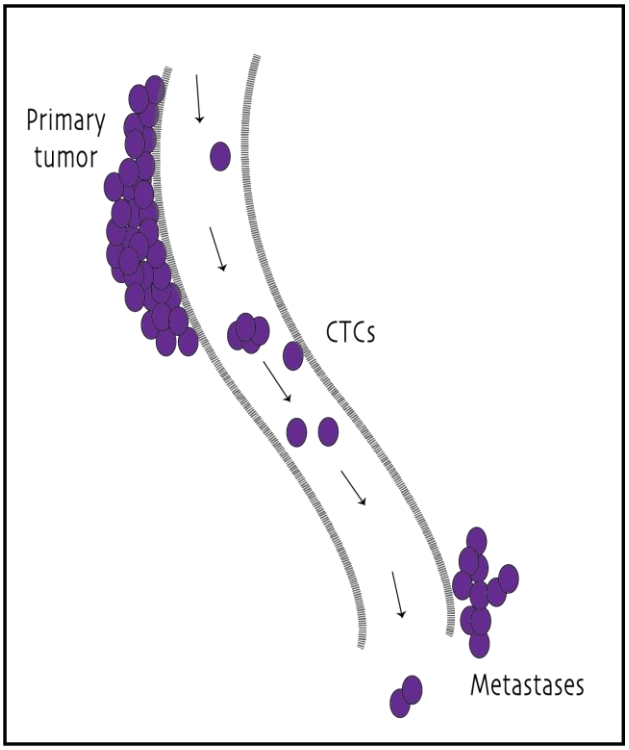

Fig 1. Figure shows detached tumor cells migrating to nearby vasculature resulting in CTCs. Resulting CTCs migrate through fluid systems to develop secondary tumors, resulting in metastasis.

At this moment there is only one FDA approved CTC detection machine, CellSearch. Detection of CTCs has been covered by a wide array of techniques, ranging from assays to microfluidics[11]. Though these techniques are partially effective, refinement of detection is still an on ongoing goal. Most importantly these techniques are not yet accurate enough to employ without secondary confirmation[12]. Multiple factors interfere with precise isolation, most of which are tied to epithelial-to-mesenchymal transition (EMT) and its reverse mesenchymal-to-epithelial transition (MET)[13]. CTCs once detached from their tumor of origin can undergo EMT and eventually undergo the reverse process of MET when attaching to a new site in the body. During these periods CTCs can be missed during detection due to their possible dichotomy. Detection techniques that seek to mark or detect only epithelial cells would miss CTCs in their mesenchymal stage and vice versa. This dichotomy has resulted in CTC detection techniques employing larger nets to collect all possible permutations of CTCs, which can also lead to a higher amount of false detections.

The current focus of the field is CTC capture and analysis. Succeeding the detection of CTCs, the issue that persists is the subsequent analysis. Often the techniques used will chemically alter or denature the cells captured. This has detracted from the ability to further understand the mechanisms by which CTCs operate and evolve. For example, detection and enumeration of CTCs before and after chemotherapy could further define the effectiveness of the treatment, but with the ability to isolate and further analyze CTCs one could possibly understand the mechanism of resistance to the drug [14,15]. Furthermore, CTCs detected in a relatively health individual, if intact, could lead to prognosis of which cancer the patient is suffering.

Prominent CTC Methods

RT-PCR is a method used in the detection of CTCs but not in their isolation. Prior to performing RT-PCR CTC enrichment is suggested. RT-PCR seeks to classify cells as malignant or normal using a range of gene expression markers. RT-PCR is a highly sensitive technique, efficient in CTC detection. RT-PCR can also be used as a post-detection method to determine cancer type and specific pathology of cancer cells. The largest barrier previously was the ability to only assay a single gene. However, through multiplexing is was determined that up to 4 genes can be assayed in a single sample[16]. Again, this method is effective in detection and even classification of CTCs, however, prior isolation and enrichment is required.

Magnetic separation, also called immunomagnetic separation, can fall under two separate categories: positive and negative enrichment. Immunomagnetic separation is the process by which cells are bound by ligands, such as antibodies, which are already attached to ferromagnetic beads. These cells, now bound to beads, are passed through a magnetic field charging their beads. Downstream the cells are pulled to one side of the flow using an oppositely charged magnet and are collected separate to the non-bound cells. Negative and positive enrichment refers to the cells which are being bound. Positive enrichment are the cells that are being analyzed, in this case CTCs. A common binding agent would be the EpCAM antigen. Negative enrichment would be binding the non-desired cells, non-cancerous cells, and common the CD45 epithelial antigen is utilized.

When referring to CTCs filtration, it is implied that one means filtration by size. CTCs by their nature are larger than normal cells in blood. Therefore, passing blood

through a filter, or even microfluidic device, allows for the separation of CTCs from normal blood particulates. Naturally, this is a passive process and therefore is less selective in cell separation. Also, this is only a form of isolating CTCs and requires further detection downstream to determine cell count. Though this method is less sensitive, it is a fairly cheap and robust method for CTC isolation. This technique fills the need of preceding enrichment in methods such as RT-PCR.

Acoustophoresis is a separation technique facilitated by acoustic radiation pressure. Matter is affected by the force of acoustic radiation when acoustic waves interact with an object in non-matched acoustic mediums. This is to say that when an acoustic wave is pushed towards an object that has a separate acoustic impedance than its surroundings. This is due to the pressure exerted on the object due to the difference in pressures that create the sound wave. This phenomenon has been exploited in filtration methods. If two particles exist in a mixture, moving those particles into a medium in which the acoustic impedance matches one but not the other allows for the application of acoustic wave separation. The particle that is not acoustically matched will be moved, by acoustic radiation pressure, separating it from the other particle. This, again, allows for positive and negative enrichment dependent on the particles that are acoustically matched to the medium. Positive enrichment being the matching of CTCs and negative being the matching of other particulates, leaving the CTCs.

Photoacoustics

Photoacoustics rely on the principle of thermal expansion and contraction. When a laser interacts with the particles in the fluidic system a specific amount of energy is transferred to the particles in the form of heat. As the particles warm, they will expand and after being removed from the laser's light they will cool and contract. This expansion and contraction, when done in a fast-enough matter, will produce a pressure wave that could eventually be collected by a transducer. There are many parameters in which photoacoustics are sensitive and are key to obtaining viable results. Most important to note is the energy transferred to the particle. The energy released by the laser must be high enough to elicit thermal expansion from the sample particle. However, it must be low enough to allow the particle to cool and contract in a manner that a recognizable pressure wave can be produced. This energy transfer is not solely reliant on the laser's produced energy but, also relies on the light absorption qualities of the sample particle. This will often lead to tagging or dying particles to allow for easier energy transfer. Finally, the pressure wave produced by the particle must be as unimpeded as possible in its travel from the sample to the transducer. Matching the acoustic impedance of the sample's solution and the surrounding area connecting the samples to the transducer is paramount to collecting viable samples.

Photoacoustics have been able to utilize the thermoacoustic response in cells to produce images. By utilizing the thermoacoustic effect expressed by light absorbing particles, researchers have been able to construct images of vasculature and other morphologies below skin surface. Molecules that are able to absorb light are used to produced sound waves below the skin. These sound waves are collected and

reconstructed. Algorithms determine placement of pixels within a defined image space which is pieced together through acoustic response. This technique has been highly effective when utilizing optically active molecules such as hemoglobin or lipids[17].

Photoacoustic Flow Cytometry is a system derived from tradition flow cytometry set ups. In traditional flow cytometry there are three main components: a light source, fluid system, and sensors. The overall process can be condensed down to particulate matter in which analysis is desired will be flowed through the fluidic system. The light source, often a laser, is focused onto a single section of the fluidics. As the particles pass through the fluidic system the photons produced by the laser will interact with optically active particles, either passing through or scattering off the particles. The sensor will then collect this information and send it for processing. Historic bench samples can be compared to the collected samples in the case of identifying unknown particles and or comparing known particles[18].

Photoacoustic flow cytometry can be considered a derivation from this process. Tradition flow cytometry would fall under the category of electromagnetic analysis. This is because the data collected and analysis conducted is centered around the photons that are either scattered, excited, or inhibited by the samples. Photoacoustic flow cytometry is considered acoustic analysis, meaning the data collected and analyzed would be on sound waves. Photoacoustic flow cytometry is conducted using the same process as traditional flow cytometry. However, the sensor used is a transducer rather than light capturing sensors. Where photosensors convert light energy to electrical energy, transducers convert sound waves to electrical energy[19].

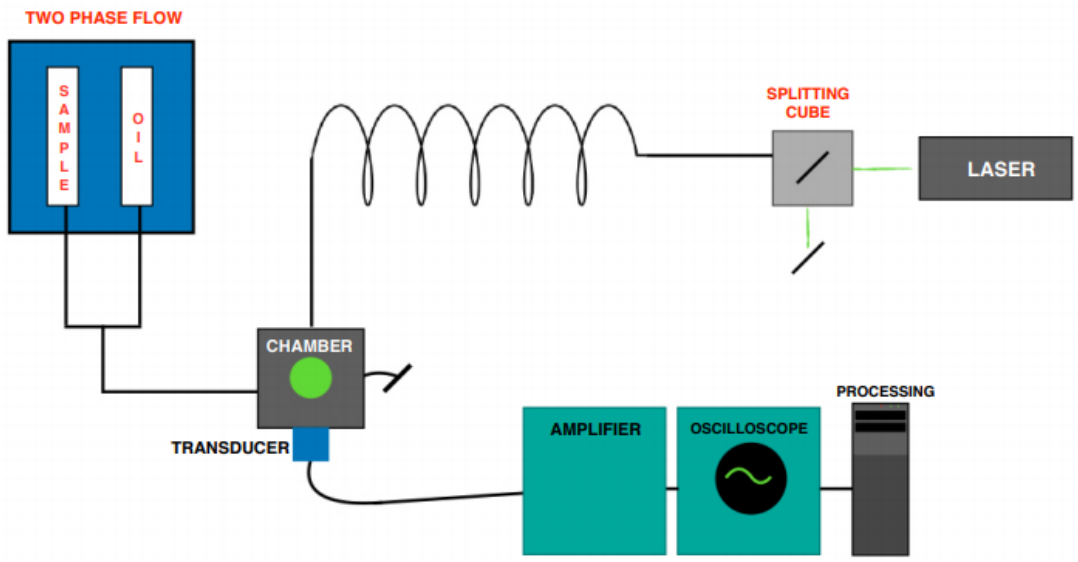

Fig 2. Schematic of Photoacoustic Flow Cytometry system composition.
System depicted is the specific system used in the following experimentation

A photoacoustic flow cytometry system is similarly composed to a traditional flow cytometry set up. A laser's energy is focused into a detection chamber. The detection chamber facilitates the interaction of the laser energy and liquid sample. In the case of the system used, a syringe pump supplies two phase flow into the detection chamber. After excitation of the sample, acoustic signals are collected by a transducer, amplified and passed into an oscilloscope for further processing (Fig. 2). Important to note is the detection chamber. The detection chamber is built specific to the focus distance of the transducer used. It is also filled with an acoustically matching medium to facilitate easier signal transfer. The fluidics housed in the chamber must be both acoustically and optically inactive to least inhibit energy transfer to and from sample.

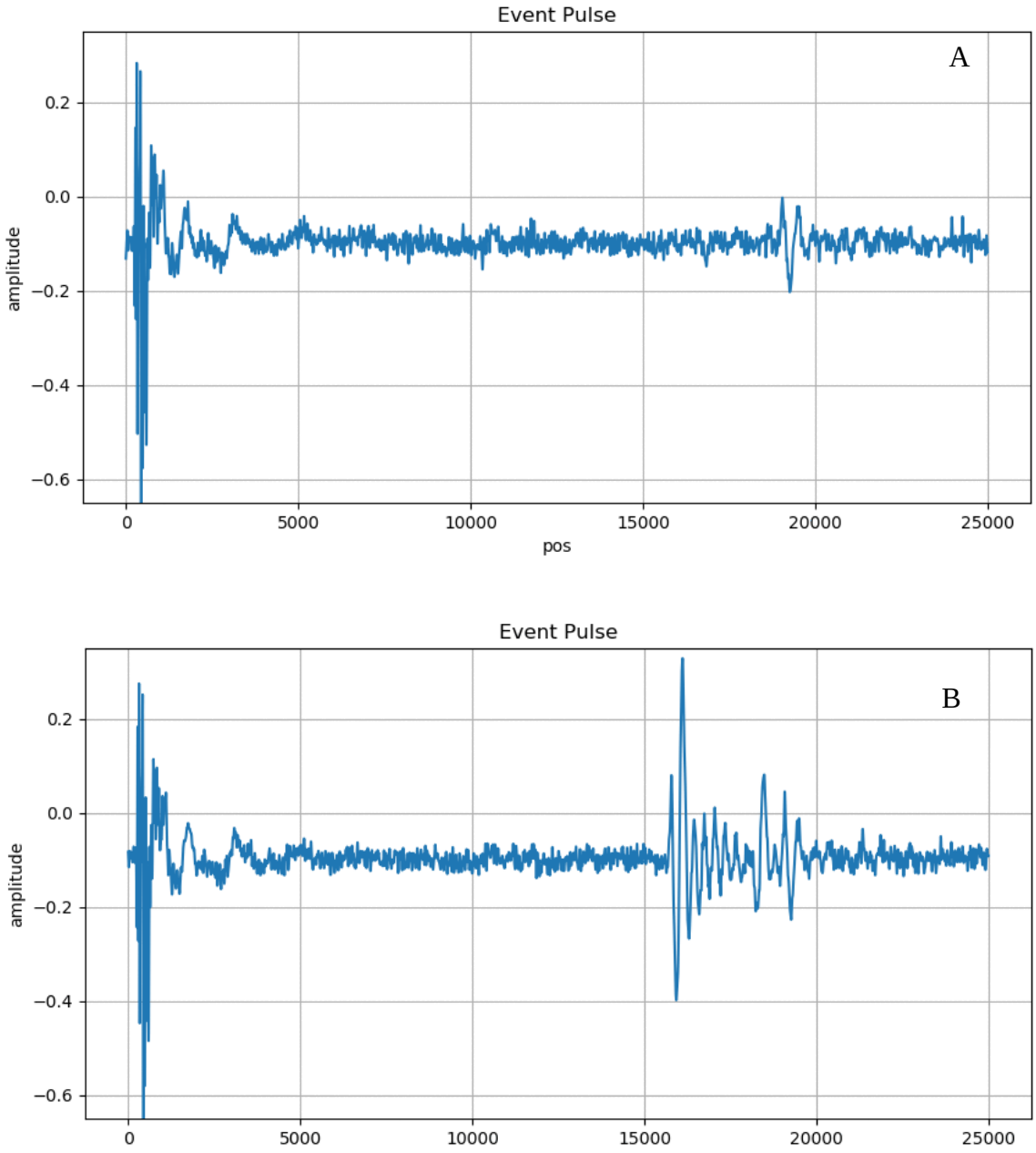

Fig 3. Waveforms of both noise and a detection are depicted. The y-axis of both graphs depicts the amplitude of the waves (mV) and the x-axis depicts the position (pos) of samples within the recorded signal. Top figure (**A**) depicts an acoustic signal from a clean chamber. Note that a large waveform is detected around position 0. This is the trigger used in laser pulsation. The second waveform around position 20000 is the "backwall" waveform. This is created from laser photons interacting with the back of the detection chamber. The bottom figure (**B**) is the same system setup but with sample detection. Note that the trigger and backwall signals remain locked in position. A third waveform present in the signal shows the possibility of detection. These waveforms are lock in positions slightly in front of backwall waveforms.

Signals produced by the system are locked to system structure. The initial reading in the waveform is the noise produced by the laser's trigger. The final reading in a signal is the laser energy interacting with the backwall of detection chamber (Fig. 3.A). When a sample produces a signal the waveform changes directly in front of the backwall reading (Fig. 3.B). The position of all these waveform origins are locked due to the distance traveled by the laser's photons. Distance between the sample waveform and chamber backwall reading is based on the physical distance between the sample present in the detection chamber and the back of the chamber opening.

Photoacoustic flow cytometry has been manipulated to present the best technique for single cell detection and capture of CTCs. Two phase flow has been introduced to the system to further separate tested samples. Alternating flow of air and sample create "slugs", which are tested for the presence of cancer cells. The samples that register acoustic signals are collected and were individually tested for pretense of melanoma cells[20]. This method was eventually updated to use mineral oil. Using immiscible liquids allows for less problematic fluidics set up while maintaining sample separation.

Photoacoustic flow cytometry has also been manipulated to allow for cell detection outside of melanoma cells. Recent research has been conducted into the possibility of detecting bacterial cells. This detection is facilitated by bacteriophage labeling. Bacteriophage that have been processed to trade their genetic material for dyes are mixed within a sample. Bacteriophage that bind to specific bacteria are given dyes unique to another bacteriophage-bacteria pair. When mixed, the presence of bacteria would cause bacteriophage to bind, effectively marking the bacteria. When the mixture is

processed aggregation of a specific bacteriophage will result in a unique acoustic response. This would signal the presence of a specific bacteria within the sample[21].

Table 1. Different attributes of common tests used in CTC experimentation.

	Speed	Capture Efficiency	Labeled	Single Cell	Automatic	Scalable
Immunomagnetic Positive Enrichment[22]	9 mL/h	70%-90%	Yes (EpCAM)	Yes	Yes	Yes
Immunomagnetic Negative Enrichment[23]	4 mL/h	79%	No	No	Yes	Yes
Filtration 8-µm pores[24]	45 mL/h	90%	No	No	Yes	Yes
Microstructure 8-µm cavities [25]	12 mL/h	80%-97%	No	No	Yes	Yes
Photoacoustic	30 mL/min	90%	No	Yes	Yes	Yes

Artificial Neural Network

Artificial neural networks (ANNs) are mathematical models that are composed in such a structure that they mimic the brain neurons of animal subjects. ANNs are composed of multiple interconnected layers composed of units called nodes. Nodes are functions traditionally comprised of a weight and activation. Information entering the node is affected by the weight, usually through a function inherit to the node type, and then applied to an "activation function" that determines the node's output. This is meant to resemble the process by which brain neurons accept, and potentially sum signals, before deciding to fire their own action potential. The layers that accept the information to be analyzed and output the model's resultant are known as the input and output layers, respectively. In deep learning models multiple layers, known as hidden layers, are placed between the input and output layers (Fig. 4). These hidden layers serve as additional signals to further the model's accuracy.

Once information enters an ANN, the data is summed and manipulated by each node in the input layer. Each node's output is then passed to the subsequent layer's nodes. In "fully connected" networks, each node passes its output onto every node in the subsequent layer. When a nodes output curls back to affect the same nodes future outputs, the network is known as a "recurrent" network. The weights are manipulated in each node to produce the networks output, meaning the training relies on manipulating nodes weights to match desired examples. This process is known as "back-propagation", the error between the ground truth and the network's output is divided among the node's weights mutating the overall model and shifting the output closer to the ground truth. This process resembles that of gradient optimization. To prevent oscillation within the model's weights, the concept of momentum is used in the back-propagation optimization

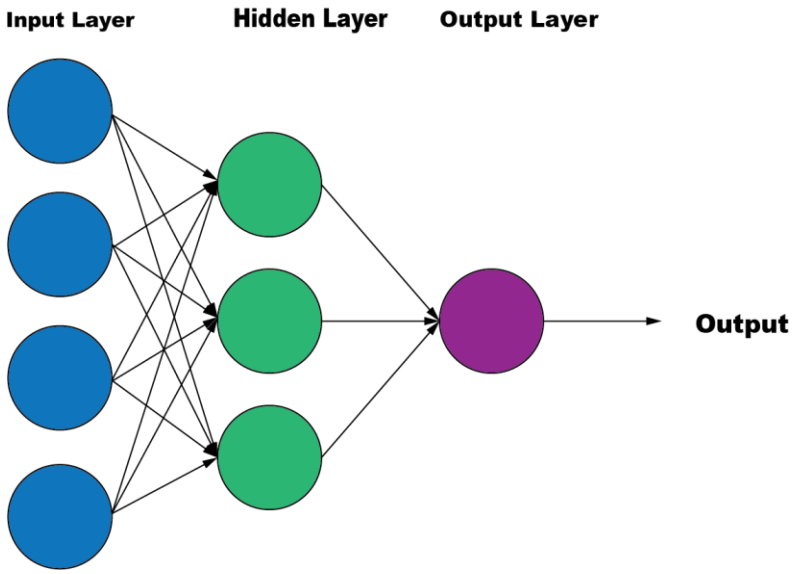

Fig 4. Traditional display of ANN construction. Input and Output layers interact with the outside while hidden layers only interconnect to model components.

function. Momentum considers the last change in a model's nodes as well as the current error[26].

The nodes that make up networks determine the processing done on the input data. Multiple different versions of network nodes exist to accomplish different tasks dependent on the initial information introduced into the model. Within this paper two types of nodes are used: dense and convolutional. A dense node is the simplest form of a feed-forward network. A dense node's function multiplies the input data by the node's weight, adds any potential bias, and passes the resultant through the predetermined activation function. Convolutional neural networks (CNNs) employ both convolution and pooling nodes. Convolution nodes employ the mathematical process of convolution in place of the dense nodes weight multiplication. This is used to reduce overfitting in the model's weight calculation. Pooling nodes work to reduce the dimensions of the information in the network. Pooling nodes reduce data by pooling the information of multiple nodes into a single node in the following network layers (Fig. 5). CNNs have been key players in image recognition models due to their ability to reduce the number of weights in a model's schema. Processing a 300x300 pixel in a dense neural network (DNN) would require the image be flattened resulting in 90,000 inputs and individual weights. By running an image through a CNN, weights can be multiplied to the image through convolution resulting in a single weight per node[27].

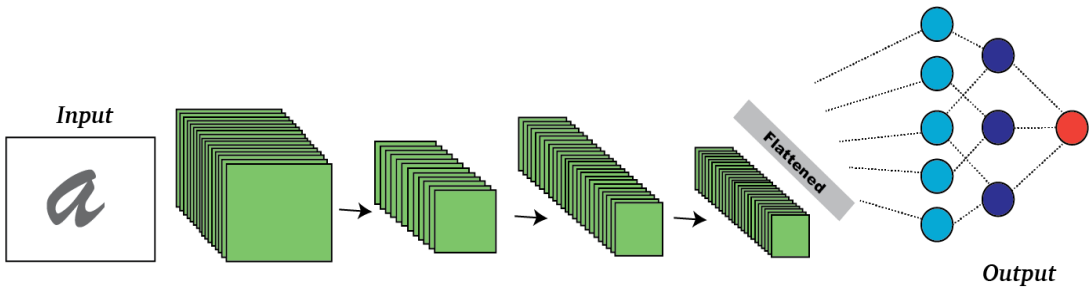

Fig 5. Traditional display of CNN construction. Convolutional layers reduce memory load by applying weights over a kernel. Pooling layers further reduce layer dimensions.

Purpose of Thesis

Photoacoustic flow cytometry has demonstrated success in detecting CTCs[28,29]. However, a more robust methodology can be comprised that allows for greater detection descriptions. By compiling a timeseries of acoustic signals, wave propagation can be determined. Referring back to the principles of photoacoustic, these waves are produced by the accumulation of thermal energy and expansion of the cell wall. Thermodynamics would suggest that these waves be determined by the ability of the cell to absorbed thermal energy and the elasticity of the cell wall. Characteristically, one would assume the walls in different cells are unique based on their composition. Furthermore, the contents of the cell would also determine its ability to absorb and disperse the energy produced by the laser. On a base level this has already been demonstrated by the lack of

stain used on the melanoma cells due to their natural pigment. The determining factor of the following experiments would be whether or not the cells have distinct enough characteristics to appear in acoustic information that can be translated by computational methods.

Regardless, neural network methods can be applied to improve the techniques already used in photoacoustics. Currently, the methodology for determining detections are thresholds. This allows for false detections in the case of debris and missed detections in the case of signals that fall below the magnitude of the back wall. By employing better post-processing techniques smaller detections can be captured allowing for finer detection accuracy. Employing deep learning techniques can also allowing for detection probability. Translating this into clinical benefits, photoacoustic flow cytometry can be upgraded into a quasi-analysis method of CTCs. With improved deep learning algorithms, photoacoustics could be used in a clinical setting for early detection CTC and disease progression analysis. With the ability to quantify CTCs in a higher-level method such as photoacoustics, preliminary results could be more descriptive and accurate allowing for faster intervention. Photoacoustics, with improved analysis, could move into other pathology detection spheres. If cell wave propagation on our current technological level is based on cell composition, that would suggest that different cells would produce characteristic waves. Allowing for the differentiation of cancer cells and other cell types.

Chapter 1

Materials and Experimental Parameters

Particles

Two types of particles were used in the following system analysis. Black dyed microspheres 0.20µm (Polybead Polysciences Warrington, PA) and HS936 human melanoma cells (American Type Culture Collection CRL-7687 Manassas, VA). Black dyed microspheres were chosen due to their use in system calibration. In previous experiments, to prepare a chamber for cell testing a strong concentration of microspheres were flown prior to data collection. The microspheres were able to induce a large response, similar to responses shown by cancer cells, and were definitive enough to assume a prepared and cleared chamber. The microspheres were suspended in a neutral density solution to create a density matched medium in which the cells would not aggregate prior to signal detection. Dilutions of microsphere concentrations were made and prior to testing cell counts were confirmed via hemocytometer.

HS936 melanoma cells were chosen due to prior experimental success in eliciting photoacoustic detections[30]. HS936 were passaged in 3mL fetal bovine serum (American Type Culture Collection Dulbecco's Modified Eagle's Medium Manassas, VA) dosed with penicillin and streptomycin, to ward off bacterial contamination during passaging. Cultures were resuspended in a neutral density solution to create a density matched medium in which the cells would not aggregate prior to signal detection. Dilutions of cell concentrations were made and prior to testing cell counts were confirmed via hemocytometer.

Photoacoustic Flow Cytometry Setup

Nd:YAG laser (Litron Nano, Bozeman, Montana) coupled into a variable beam splitter (VA5-PBS252 Thorlabs Newton, New Jersey), reducing output from 4mJ into two equal 2mJ beams. Resulting beam is coupled to a 1000μm, 0.39 numerical aperture, optical fiber (Thorlabs, Newton, New Jersey). Laser beam was composed of 532 nm laser light, pulsed at a 5-nanosecond rate. The laser beam energy coupled through the optical fiber was maintained and measured from to 2 mJ for experiments. Laser light was directed to a quartz tube (Quartz 10 QZ,124Charles Supper, Natick, Massachussetts) with 10μm thick walls. The 10μm thick walls allow the propagation of ultrasonic waves, as well as providing an optically transparent pathway for the sample to flow through. Optical fiber was placed 5 mm from the quartz tube to create a detection volume of 0.04μL. A 2.25 MHz transducer focused on the quartz sample tube was fitted to the base of the flow chamber. The internal volume of the chamber was filled with Sonotech LithoClear acoustic gel (NeXT Medical Products Company, Branchburg, New Jersey) to provide a medium for the propagation of acoustic waves. Syringe pumps were used to create an alternating flow of sample and mineral oil equal to 60/min flow rate. The introduction of sample and the immiscible mineral oil induced two-phase flow. Two-phase flow was employed to allow for future collection of the samples for further analysis, while eliminating the possibility of samples becoming stuck or delayed inside the tubing. Signals were amplified with a gain of 50 using a Tegam 4040B amplifier (Tegam, Inc., Geneva, Ohio) and sent to a desktop computer running a customize python program. The python programed served as the data collection and differencing detection method modality. This flow chamber setup served as the excitation and acoustic wave

collection device. Signal is collected by the transducer and transferred to an amplifier (Tegam 4040b) which multiplies the signal 100 times. A signal sample is collected every 50 milliseconds. Each sample is composed of 25000 data points that correspond with the laser light's speed from the laser to the back wall of the chamber. Hallmarks of a signal are the trigger wave and backwall wave. The backwall is created by the laser light interacting with the back of the chamber structure. Detection pulse exists immediately prior to the backwall signal. Detection pulses are location based and will remain locked in the single position that corresponds with their physical location in reference to the photons time of flight.

Custom Programming

Custom programming was written to replicate a previously LabView based program. The translated program, developed on a Python framework, replicates the traditional detection strategy and employs a secondary detection strategy for comparison. By using the traditional detection method as a standard, effectiveness of differencing detection methodology can be assessed. The tradition detection strategy was a dual threshold-based strategy. The signal received from the transducer was based on the manipulation of an AC signal. Therefore, acoustic waves could disrupt the base signal in both positive and negative directions. This created cause for dual thresholds both based on a positive and negative .01 reading. Signal sample was reduced to readings immediately preceding the backwall signal and top and bottom thresholds were manually adjusted to account for noise strength. Adjustments are insignificant to overall detection thresholds.

A secondary detection methodology was developed to improve upon the traditional method. A sample signal was again reduced to the sample points immediately preceding the backwall signal. The absolute difference between the current and leading signal was calculated and any change over .002 was assumed to be a wave change. A signal was assumed to be booked ended by two wave changes, initial propagation and signal rectification. This assumption was based on empirical observation (Fig. 6).

Detections were based on the improved detection philosophy. This is due to the problem of saturation. In instances of high concentrated microsphere sampling, multiple microspheres can be present in a subsample at a single point in time. This saturates the transducer and changes the overall sensing environment (Fig. 7). Signals would change from manipulating a basic noise signal to a saturated noise signal. Both environments display a detection, however, sub detections arise within the saturated noise signal and can be further classified. To allow for detections of these sub signals, the improved differencing methodology was devised. Both detection methodologies were practiced on the sample signals and were later compared.

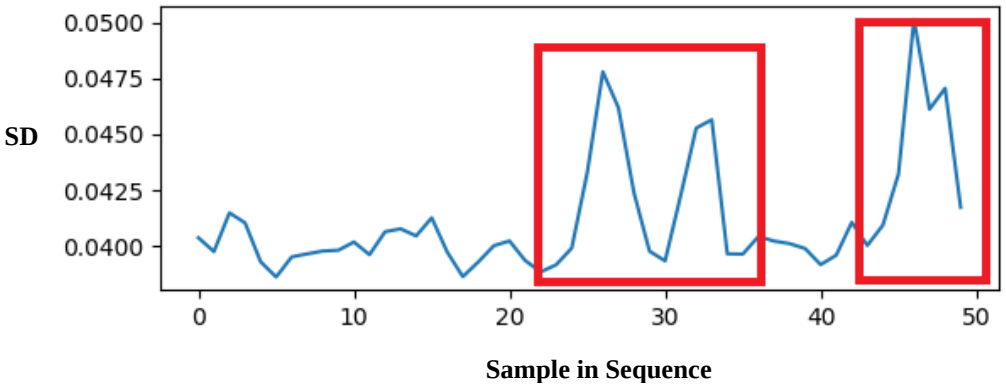

Fig 6. Display of standard deviations of multiple signal samples in time series. Marked events are changes in deviation attributed to signal propagation and signal rectification.

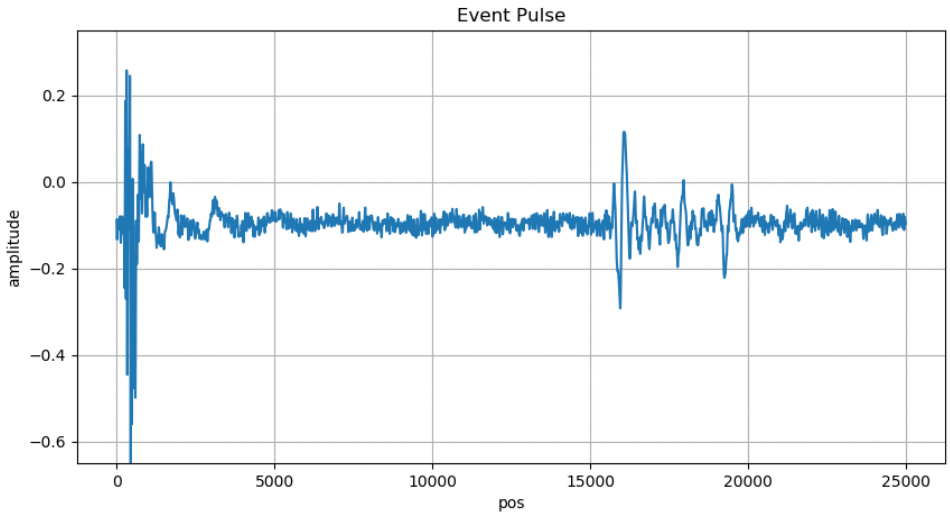

Fig 7. Saturated waveform. Similar in visual to a detection, saturated waveforms remain in this shape over multiple samples due to particles creating a constant base signal.

Chapter 2

Experimental Procedure

Initial particle concentrations were determined prior to all sample runs. Each sample produced consisted of a single milliliter of fluid, flowed through the system in two phase flow with mineral oil. Each sample syringe was primed with a small amount, less than half a milliliter, of mineral oil to produce a complete seal with sample and plunger. All samples were suspended in a solution of respective neutral density buffer to prevent aggregation prior to testing. Laser energy was tested and confirmed to be 2mJ of 532 nanometer light. Acoustic gel within chamber was de-bubbled by hand to produce the path of least impedance for the acoustic signal and reduce debris noise within captured waveforms. All tests were run in the same timeframe and theoretically the same acoustic gel composition. This was done to reduce the variation in noise between sample runs. Test concentrations of the highest quantity cell count of both HS936 and microspheres were run prior to recording. This was done to confirm the efficacy of signal production from the sample cells.

Twelve trails were run in alternating order. Six trails of different dilution HS936 cells and six trails of different dilution microspheres. Trails were conducted in descending particle concentration order, highest concentration of particles to lowest concentration. After each run PBS was flushed through the system to determine clean tubing and a clean chamber. Chamber cleaning was visually confirmed by signal normalization. Samples for HS936 and microspheres began at 375,000 cells per milliliter and 300,000 particles per milliliter respectively. Each trail particle concentrations were halved. The detections were recorded for the top three concentrations for both particle

types. In total 3,350 separate waves were detected, 1,368 HS392 detections and 1,982 microsphere detections.

Chapter 3

Methodology of Post Analysis Techniques

Dense Neural Network Classification

The overall goal of this study was to assess the possibility of classifying CTC signals from the signals of other particles. Thus, increasing the accuracy of photoacoustic CTC detection by eliminating false positives. Neural networks were leveraged as a primary line of attack in this investigation. Neural networks, in a classification construction, train themselves to assess every aspect of input signals and best classify based on provided information. By giving the networks the raw data and their ground truths, any possible differentiation in the signal can be exploited through training. Dense neural networks (DNN) are best equipped to handle one dimensional data. The peak signals, signals of the highest response, within the recorded events were parsed and assumed to be the representative sample. These samples were introduced to a dense neural network to assess the possibility of single signal classification. It is important to note that in every neural network case there was preprocessing of data before introduction into the network, except for the case of DNN classification. Pre-scaling of the signals produced no reliable outcome in preliminary exploration. The assumption made was that there are no real differences inherit in HS936 and microsphere single sample signals other than magnitude (Fig 8). Autoencoder constructions of DNN networks were also tested and will be further explained later in the paper.

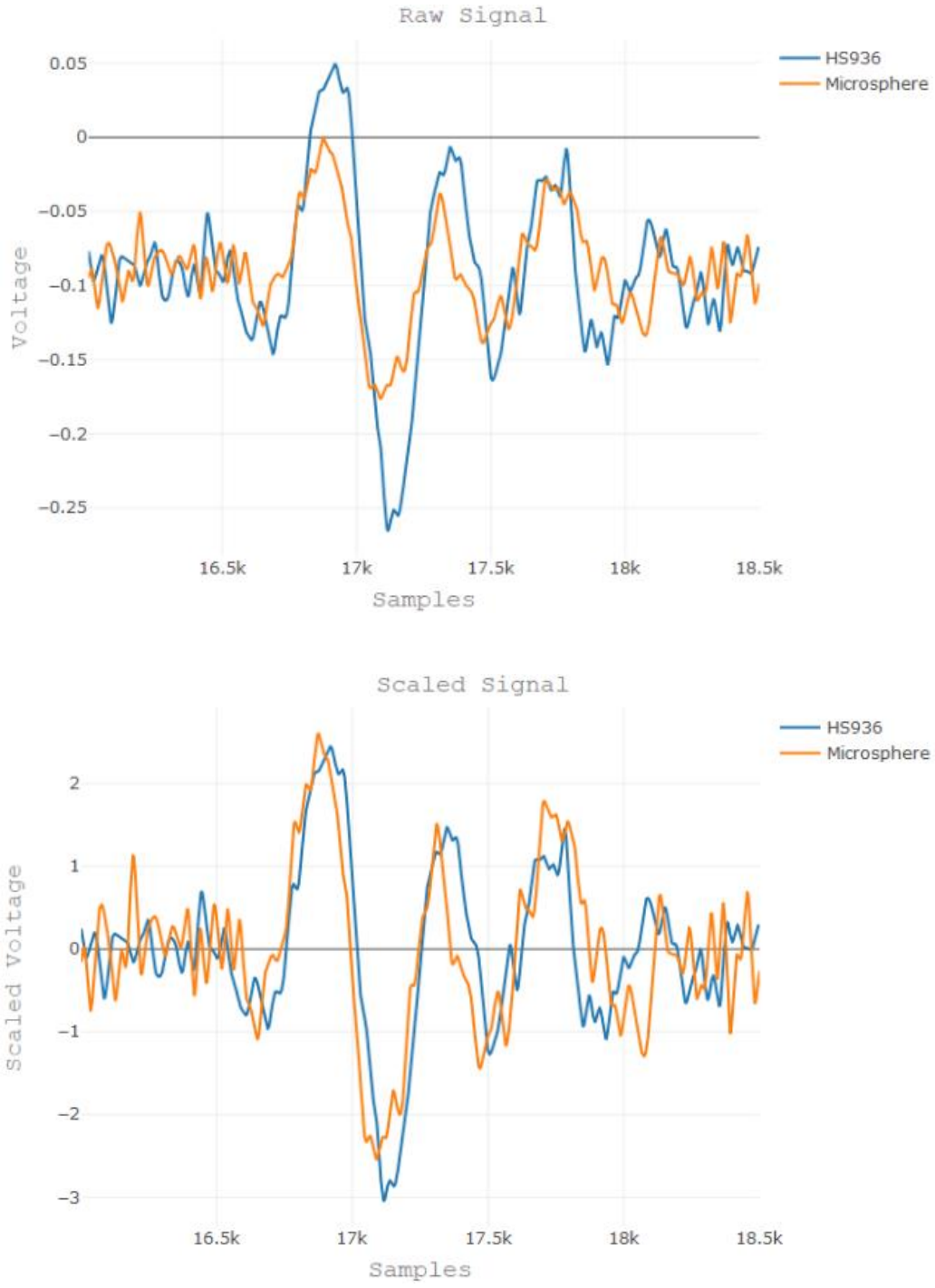

Fig 8. Comparison of HS936 and Microsphere signals before and after scaling. Peak raw signals maintain similar morphology while differing in amplitude. After scaling signals are indifferentiable. Amplitude is measured in mV; "Samples" refers to the data point's position within the larger signal.

Convolutional Neural Network Classification

Convolutional neural networks (CNN) excel in image processing. The nature of the event signals, though time dependent, can be manipulated into an image. The images can be viewed as heatmaps but are better displayed in surface plot constructions. To eliminate the potential of oscillation within the model training all data points within event signals are squared. This removes the potential for oscillation around zero and amplifies the acoustic waves while lowering noise. Smoothing is applied over every sample within the event. This further removes noise and adjusts the digitized wave to a more natural analog formation (Fig. 9 & 10). Initial hypothesis assumes CNNs would have greater classification ability than DNNs. Though the peak signal of an event may be representative, including the surrounding events allows for consideration of wave propagation.

Autoencoder Construction and Usage

Both DNN and CNN autoencoders were developed to assess inherit differences in wave morphology. Autoencoders efficiently reduce the dimensionally of input data. If any difference were to exist within the HS936 and microsphere wave forms, two different clusters would form in the resulting graph. Further algorithms could be run on the new data, such as centroid nearest neighbor algorithms, to determine further classification. This is one of the key points of discovery within the following experiments. Neural networks are powerful enough to devise classification by leveraging non-replicable data. Also, even if classification is possible, new models would need to be built and trained for each new particle that one would desire to classify. Classification models are the more robust and realistically the only reliable way, aside from mathematic methodology, to

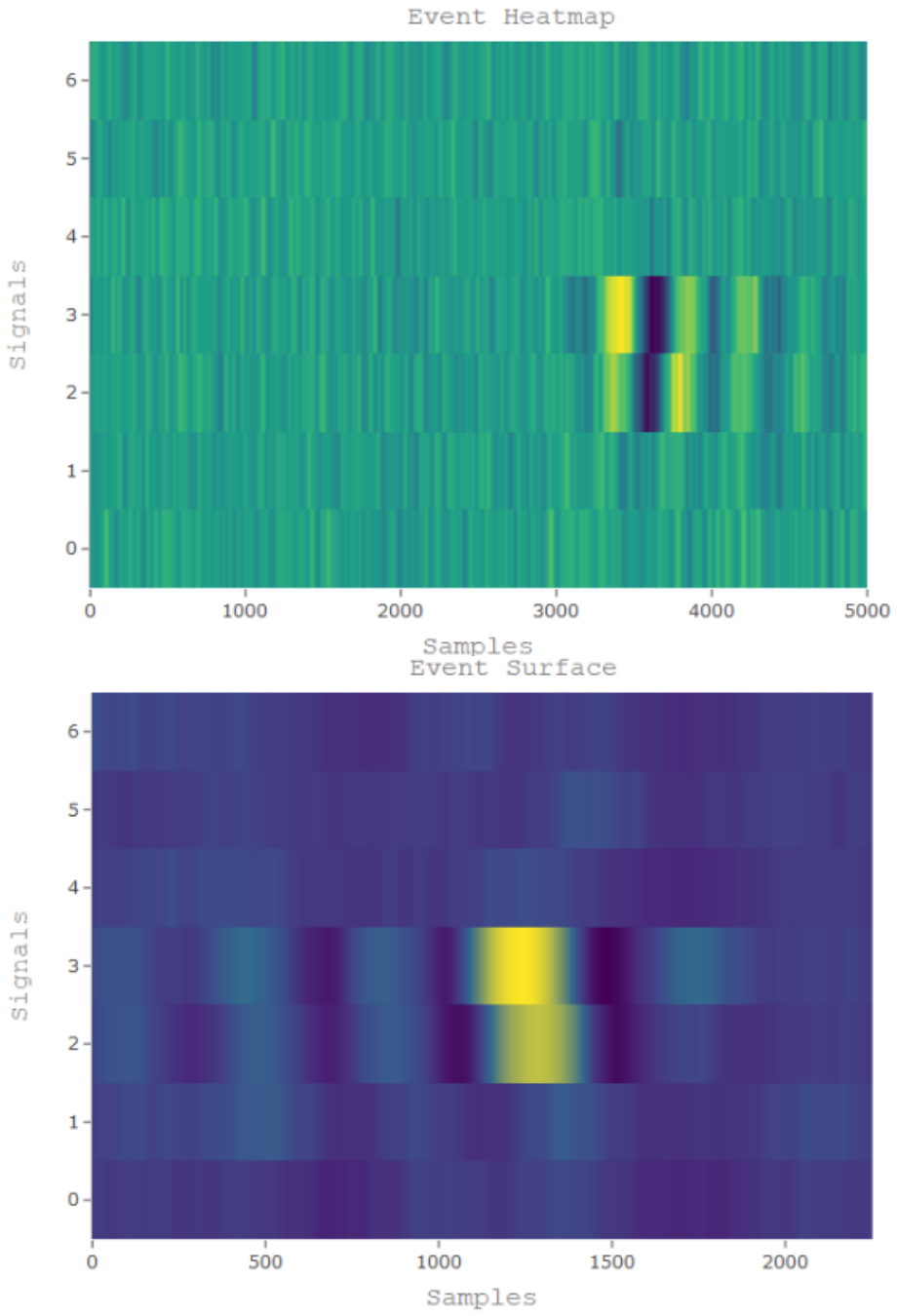

Fig 9. Detection event before and after squaring in heatmap form.

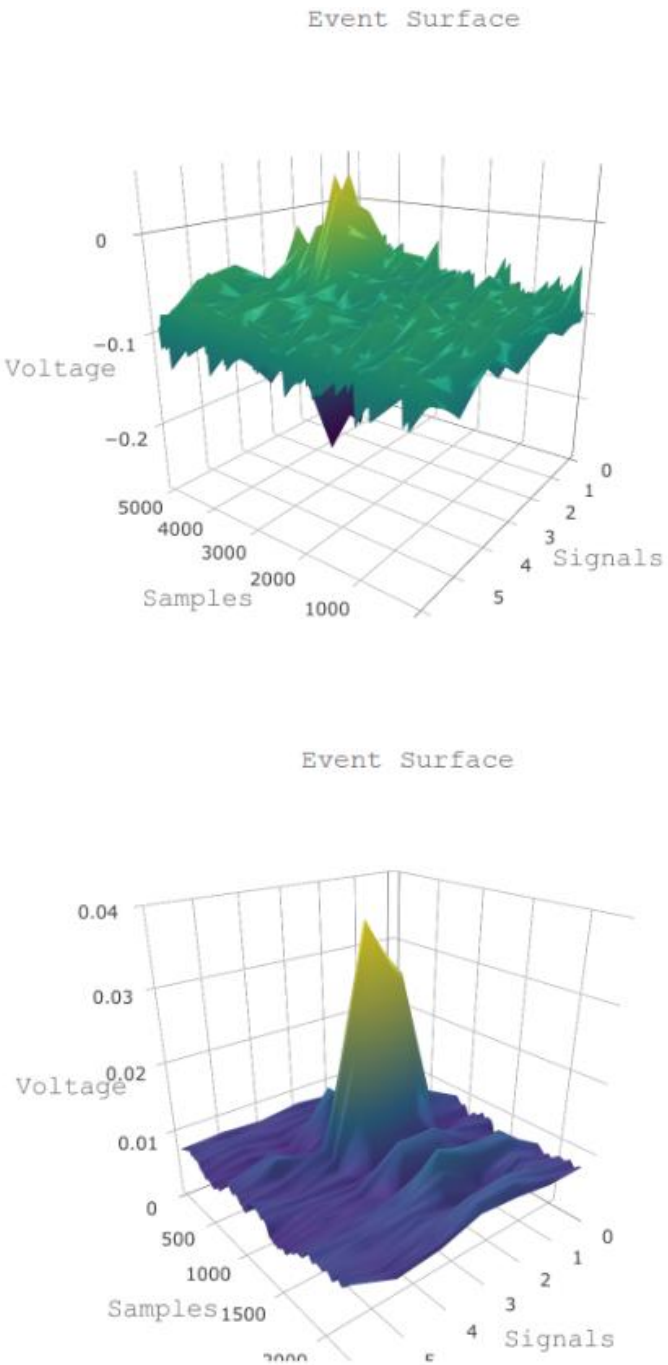

Fig 10. Detection event before and after squaring in surface plot form.

confirm unsupervised classification in a clinical sense. However, from a research standpoint, autoencoders offer much more information about that particles than merely classification. By developing an autoencoder model, a potential feature map can be devised on which other waveforms can be placed. By running an untrained signal through the model, that is neither HS936 nor microsphere, a point would be placed based on some inherit waveform characteristic. By determining the characteristics on which the waveforms are reduced, a classification map of cell response could be developed. Allowing for a future unsupervised classification of particles.

Neural Network Bootstrapping

Bootstrapping is a common data mining technique that allows for statistical determinations to be derived from smaller amounts of data by random selection with replacement. By resampling data from an initial population, a secondary representative population can be established and assumed similar enough to the original data to make further assumptions. A key problem with this type of inference is the potential of representation saturation, there may be some samples that are represented higher in the original sampling than in the true population. By bootstrapping, that representation can be over assumed, and untrue inferences can be drawn.

In an attempt to discern overrepresented features within waveforms, representation saturation is leveraged by randomly producing multiple machine learning models and testing their ability to classify signals. Neural networks are intentionally tuned to learn off of specific datasets. However, in the instance of exploratory classification, by utilizing randomly generated neural networks one could assess the robustness of a dataset’s inherit features. If classification is possible, that suggests a

strong inherit difference in tested signals that should be further explored for fundamental structural differencing. Restrictions by which the models were developed can be found within the supplementary information. 100 randomly generated models for both constructions, classification and autoencoding, were developed for both DNNs and CNNs.

Fundamental Analysis

Parabolic wave reconstruction was done to establish a high-fidelity waveform. With a higher fidelity dataset, fundamental analysis was done on waveform morphology. By mutating techniques used in mass spectrometry, specifically the concept of peak resolution, novel values were obtained and could serve as the underpinning of neural network classification. Parabolic extensions were accomplished in both array dimensions beginning first with samples points then event samples. This was done to create a stable base on which a larger extension assumption was calculated. Each dimension was extended by 100 times their original length. Parabolic extension was chosen based on the assumption of laminar wave propagation. The final reconstructed wave in the sample direction was pooled by a kernel of 2,100. Specifics of the extension algorithm are found in the supplemental material.

Chapter 4

Results of Network Classification

DNN Classification

Single peak DNN classification was used to determine the possibility of single wave classification. Non-scaled max peak signals were chosen from event detections as the representative wave form within the event. Base DNNs were constructed to assess the most viable structure from which model randomization could occur. DNNs were trained to classify representative signals, cancer signals being trained as scoring one and microsphere signals trained as scoring zero. Rectified linear units (ReLU) were chosen as model activation functions to map results between zero and positive infinity. This mapping was chosen to allow the model to express percent chance of classification. Outputs from the model would represent the percentage chance of being classified as a HS936 cell signal. Overall model performance was calculated by pure success, number of samples that represent ground truth divided by total number of samples. The mean performance in each trail of all models appeared to score relatively high on with a pure success calculation (Fig. 11.A). However, viewing the distribution within model scores revealed a wide range of variation. This would suggest instability in model structure or data composition (Fig. 11.B). Prior observation suggests a lack of difference between scaled signals, creating a need to classify unscaled signals. Peak signal distribution shows small variation range with high similarity between trails. This would cause model confusion in signal differentiation.

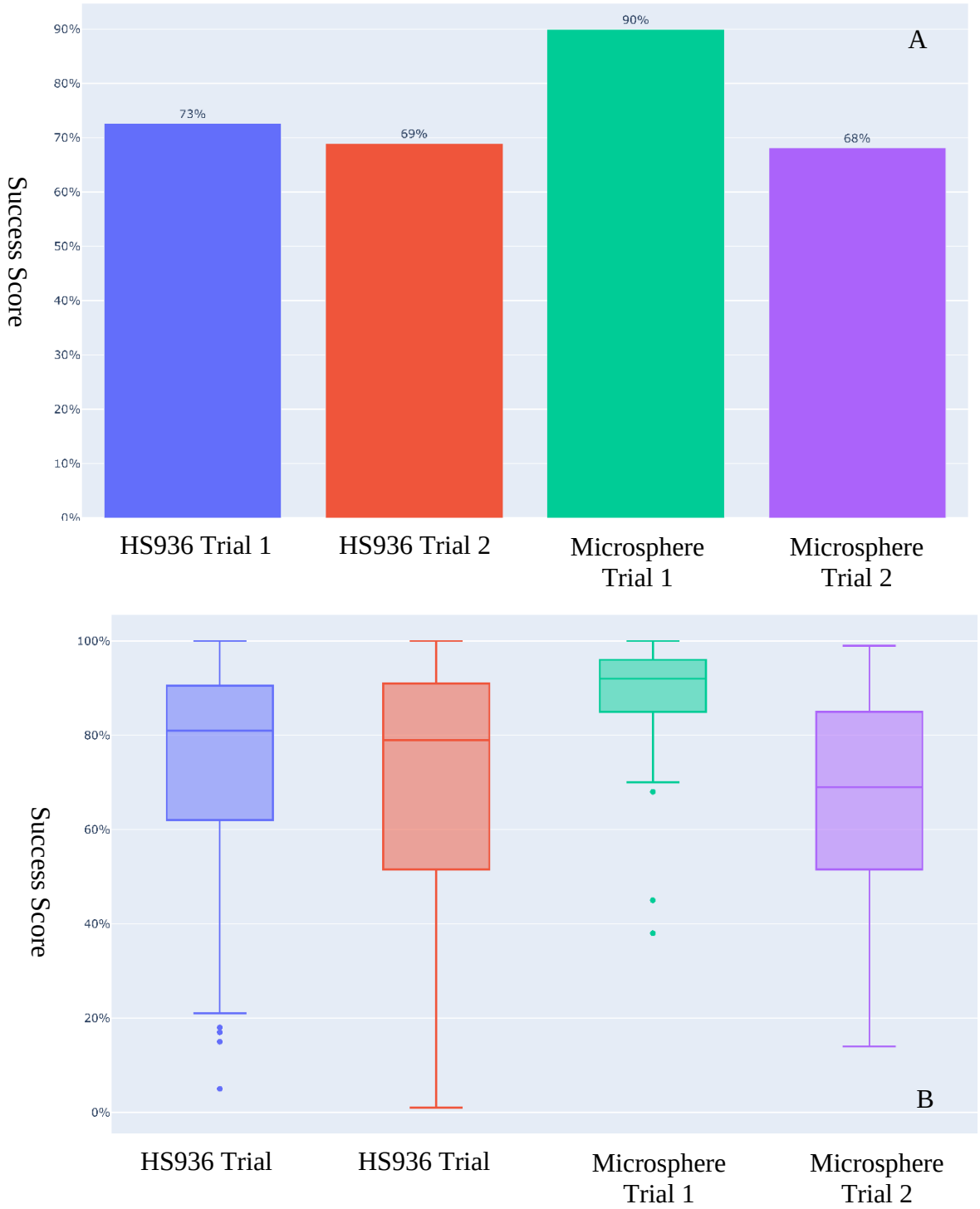

Fig 11. Average success ratings for all randomly generated DNN model for single wave classification displayed promising results. (A) However, the distribution of the model scores suggests alternation in model success, some highly accurate in cancer classification and some highly accurate in microsphere classification. (B)

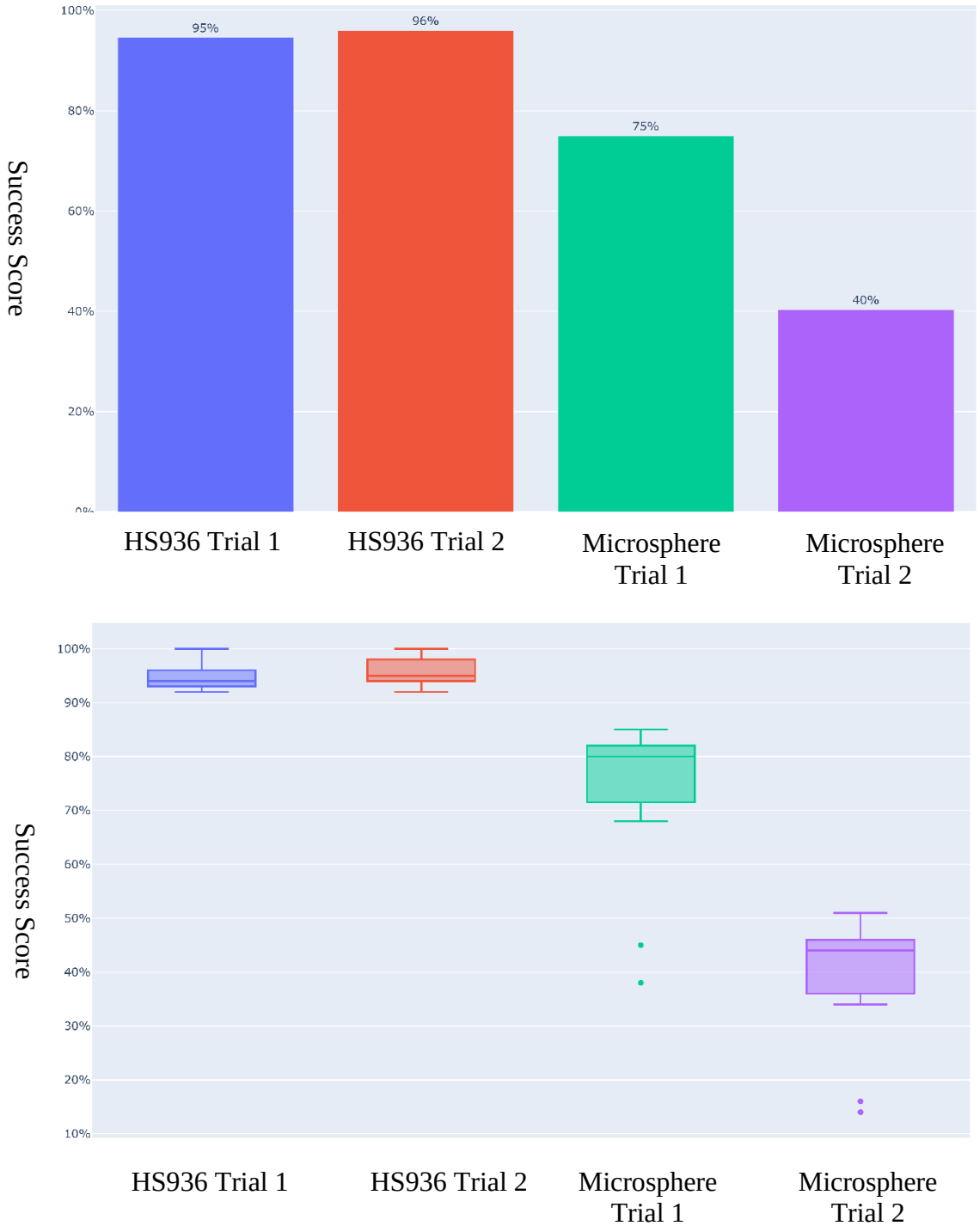

Fig 12. Sorting the models based on cell type classification success and polling the top 20 models displays alternating nature of testing success. Near half the models trained to accept all signals above differencing threshold of 50%. Showing high success in cancer classification.

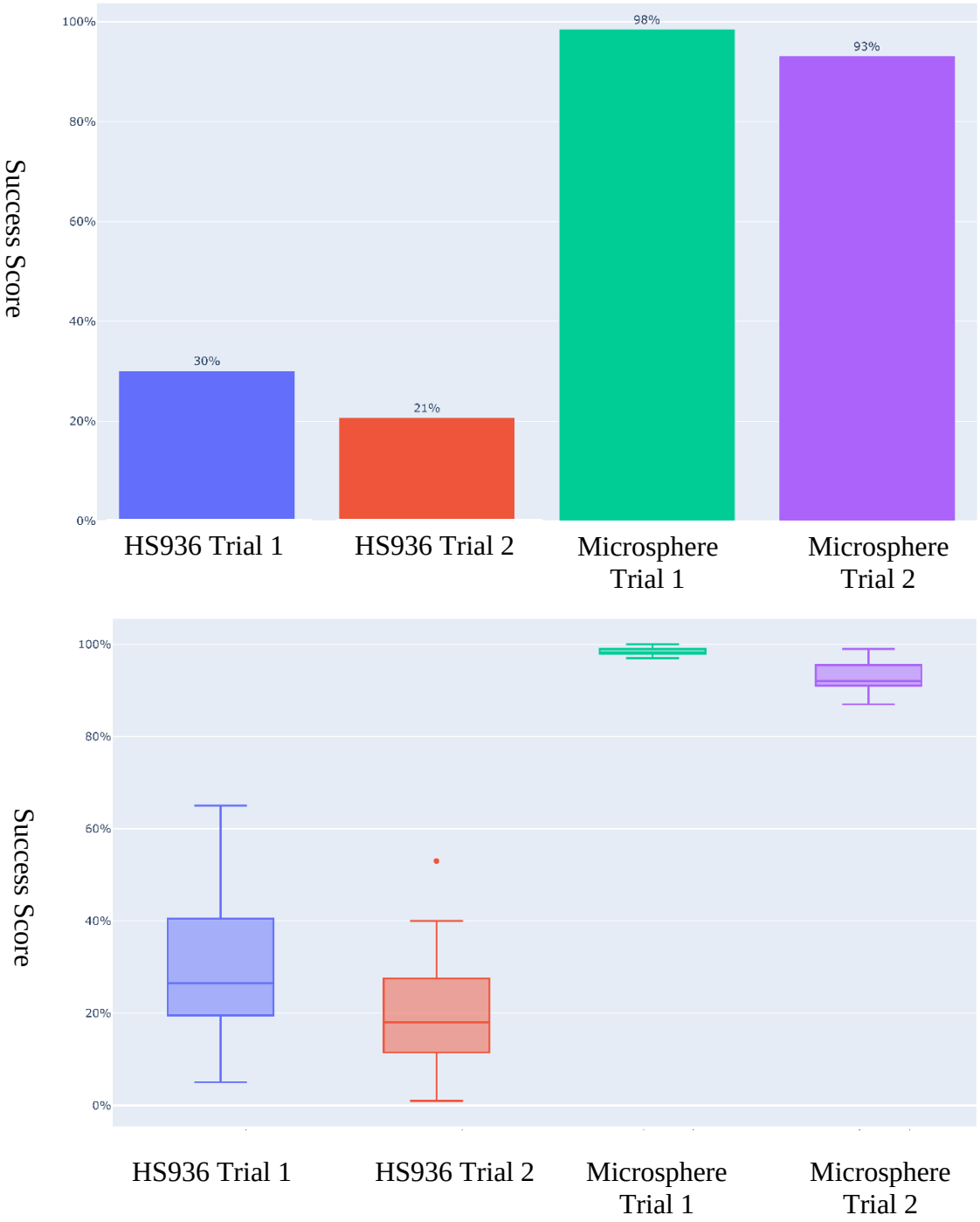

Fig 13. The microsphere-based model grouping pulled all values below 50%.

Further investigation revealed models were almost evenly split between favoring cancer or microsphere wave morphology (Fig. 12 & 13). Selecting the top 20 highest scoring models sorted by HS936 classification success depicts a model that pulled signal score above classification threshold (50%). By pulling all signals above or below the signaling threshold, a model with high success in either cancer or microsphere categories would be created. This would cause the misrepresentation of success in overall model calculations. Polling top 20 microsphere score models shows a similar but opposite response.

What is of note in the models, though unable to accurately classify based on a single wave peak, is the pull of signals during classification. In both cancer and microsphere model's cell types are not completely confused. Though the features detected are not strong enough for efficient classification, modeling shows distinctive differences within peak waves (Fig 14). However, this difference could be represented by the magnitude of each wave type, due to the lack of pre-scaling. Evaluation of single wave distribution does not show significant distribution shift in magnitude, but previous scaled tests suggests strongest differencing relies on wave magnitude (Fig 15).

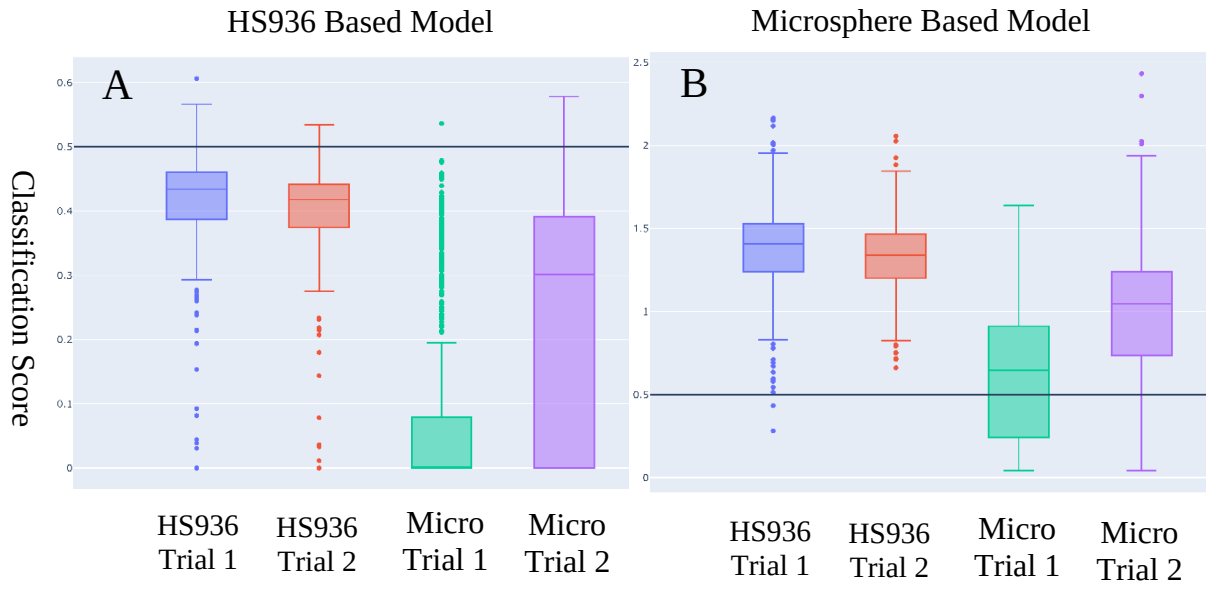

Fig. 14. Though unsuccessful in direct classification model distributions suggest novel differencing within peak waveforms. Horizontal line in graph depicts difference threshold 50% (.5). Though cancer models pulled all values about detection threshold, microsphere samples are notably spaced from cancer samples. (A) The same response is observed in microsphere model with cancer samples pulling closer to classification threshold. (B)

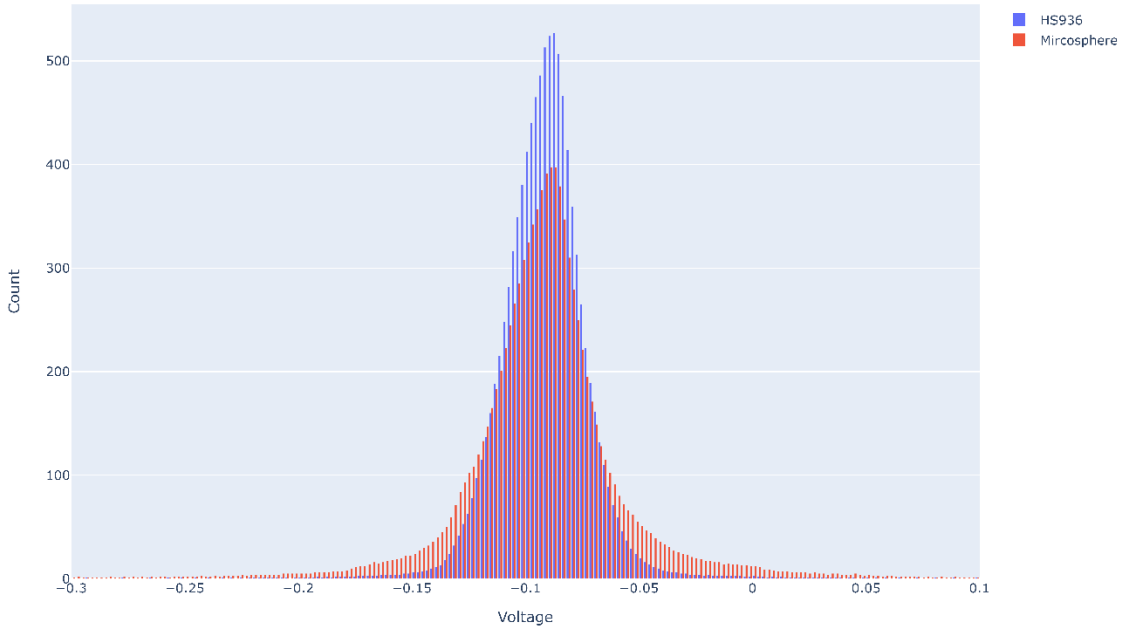

Fig. 15. Investigation of wave point distributions showed no notable shift in magnitude, suggesting pull factor relies in wave morphology.

CNN Classification

CNN classification was used to assess the potential of event classification. By including the surrounding signals of a peak wave, the hypothesis is that wave propagation would be including in feature classification. Similar to DNN classification, ReLUs were used as the activation function and outputs were tied to positive values to represent percentage chance of classification. Unlike DNN classification, input event signals were smoothed and scaled. Smoothing the signals reduces digitization of the signals and the potential of noise being chosen as a feature for classification. Based off pure success calculations of 100 CNN models, model classification is improved with surrounding event inclusion. Analysis of variation shows overall calculations are consistent with model success distribution (Fig. 16).

To assess the possibility of selectivity, top 20 models for both HS936 and microsphere success were checked. Selectivity was again observed, present assumption is that models chose a signal to act as a base by which difference was calculated. Selectivity in this case was not detrimental in overall classification (Fig. 17). Models based on microsphere classification, assumed to be models with higher microsphere classification scores, scored much lower on HS936 classification than the opposite case. This suggests models in which HS936 are interpreted as the base signal are superior for classification.

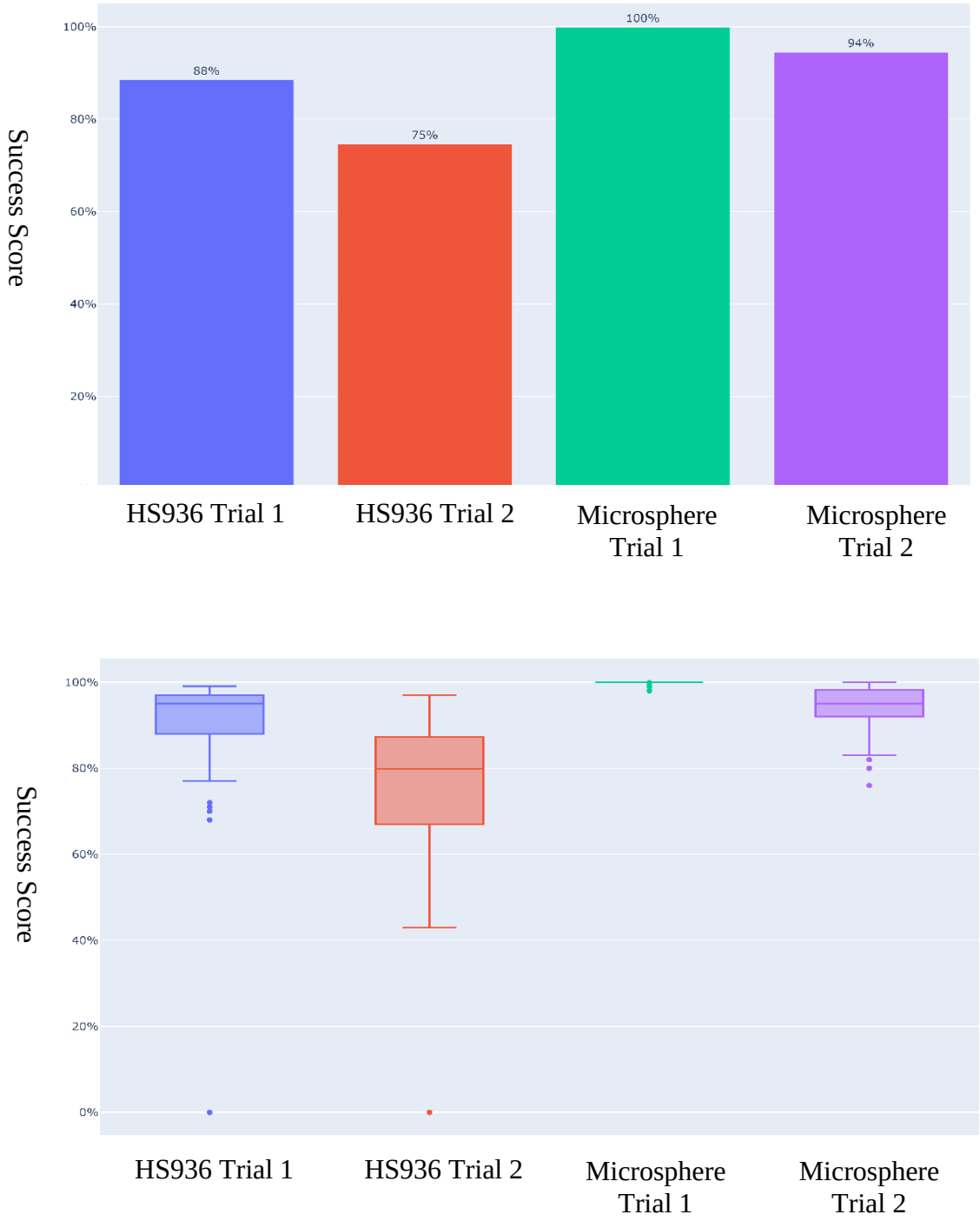

Fig 16. 100 randomized CNN classification model success calculation. Average result and distribution.

Pull during classification was again present suggesting similarity in wave morphology (Fig. 18). The possibility of wave magnitude, though inputs were scaled, could present as the pull factor. The difference in pull factors between DNN and CNN classification could be the overall points observed. With the larger array of data, overall event magnitude could be diluted and therefore model pull lessened.

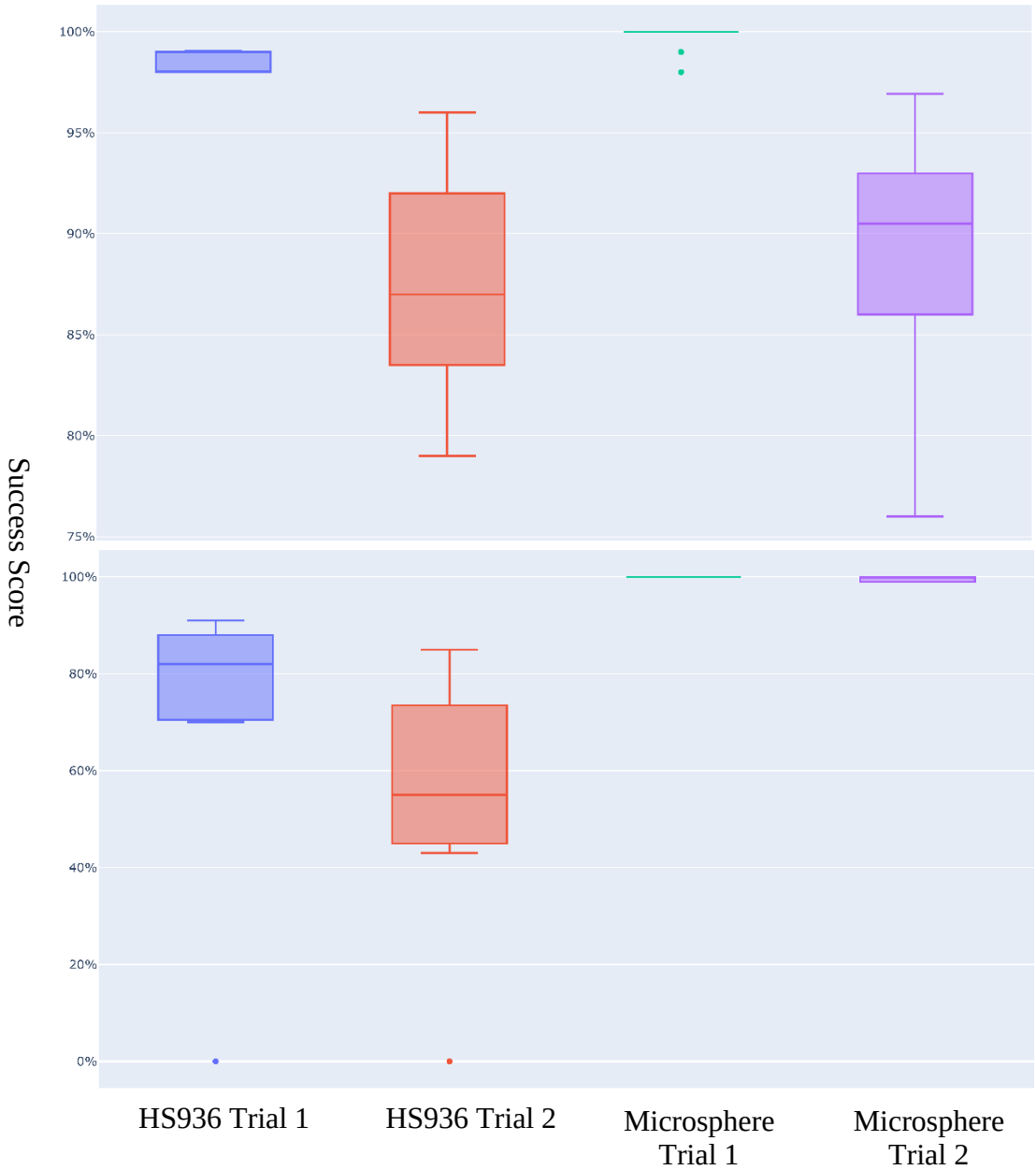

Fig 17. Left graphs depict top 20 cancer models and right graphs depict top 20 microsphere models. Success distribution shows selectivity but model success is much less effected.

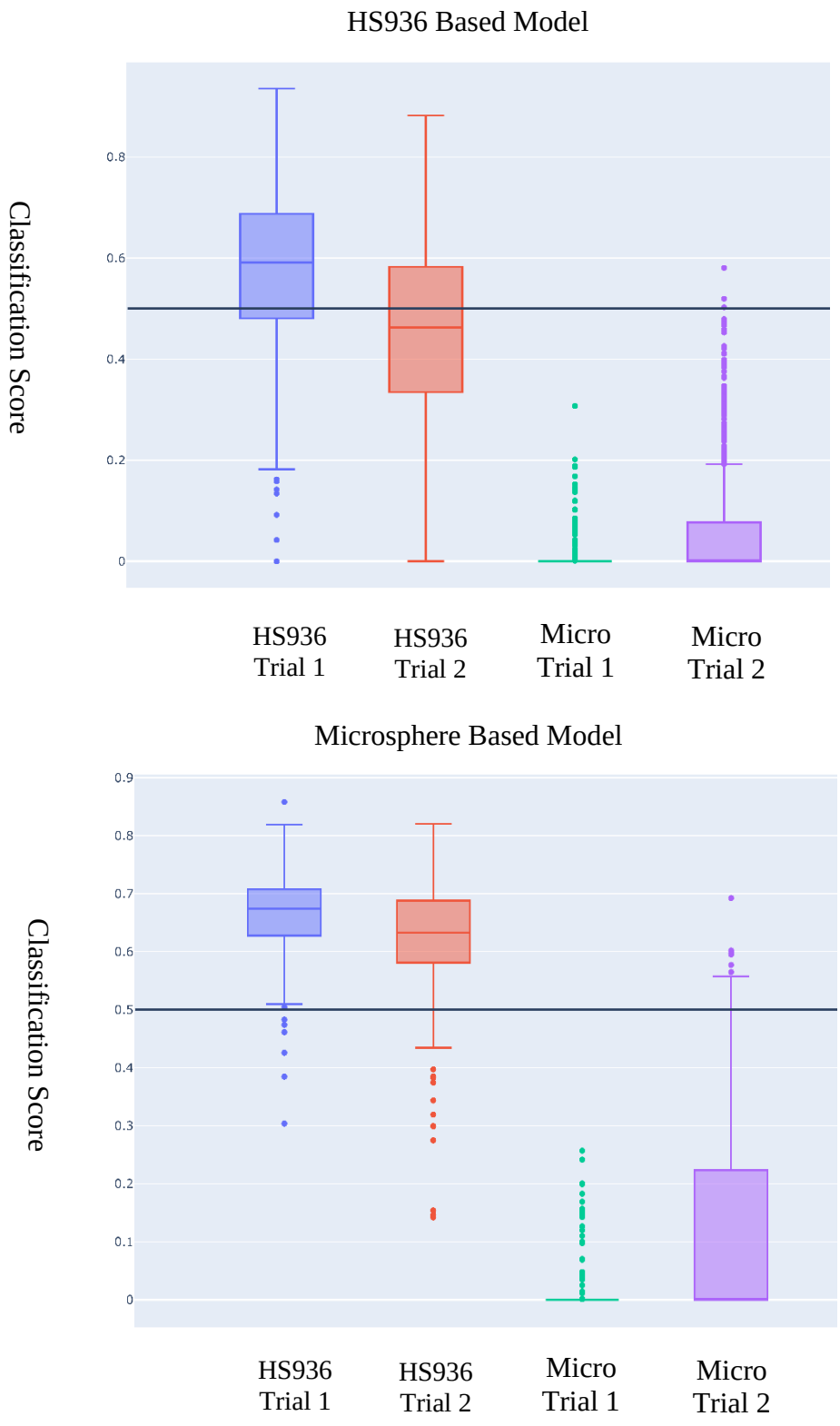

Fig 18. Pull is still present in classified samples, just to a lesser degree. Assumption is the amount of data used in CNN classification diluted pull factors when training.

Chapter 5
Results of Autoencoder Networks

DNN Autoencoder

Autoencoders were chosen to assess the potential to create feature maps on which unclassified events could be placed to depict insight in unknown cell thermoacustic response. DNN acutoencoders were used to determine the vaibility of single signal dimensional reducution to feature map. As with DNN classification peak signal was chosen within an event to be the representative waveform. By the nature of autoencoders the singal strength of raw singals were not larger enough to adequatly map features, because of this signals were scaled before input into the autoencoder. Signals were reduced to coorinates by ReLU activation. Coordinates were plotted and centriods of trails were determined. Classification success was determiend by euclidean distance calculation from centriods.

DNN autoencoder classification was poor, barely succeeding over half the samples (Fig. 19). Varition within models is consistent with overall scoring. Tukey Post Hoc analysis was conducted on the difference in trail coodinate interaction to determine significance during direct popluation comparison. ANOVA analysis was discarded in favor of Post Hoc confidence intervals. Intervals displayed show the mean difference within populations. Trail conparisons in which population mean difference hovers around zero suggests significantly similar populations.

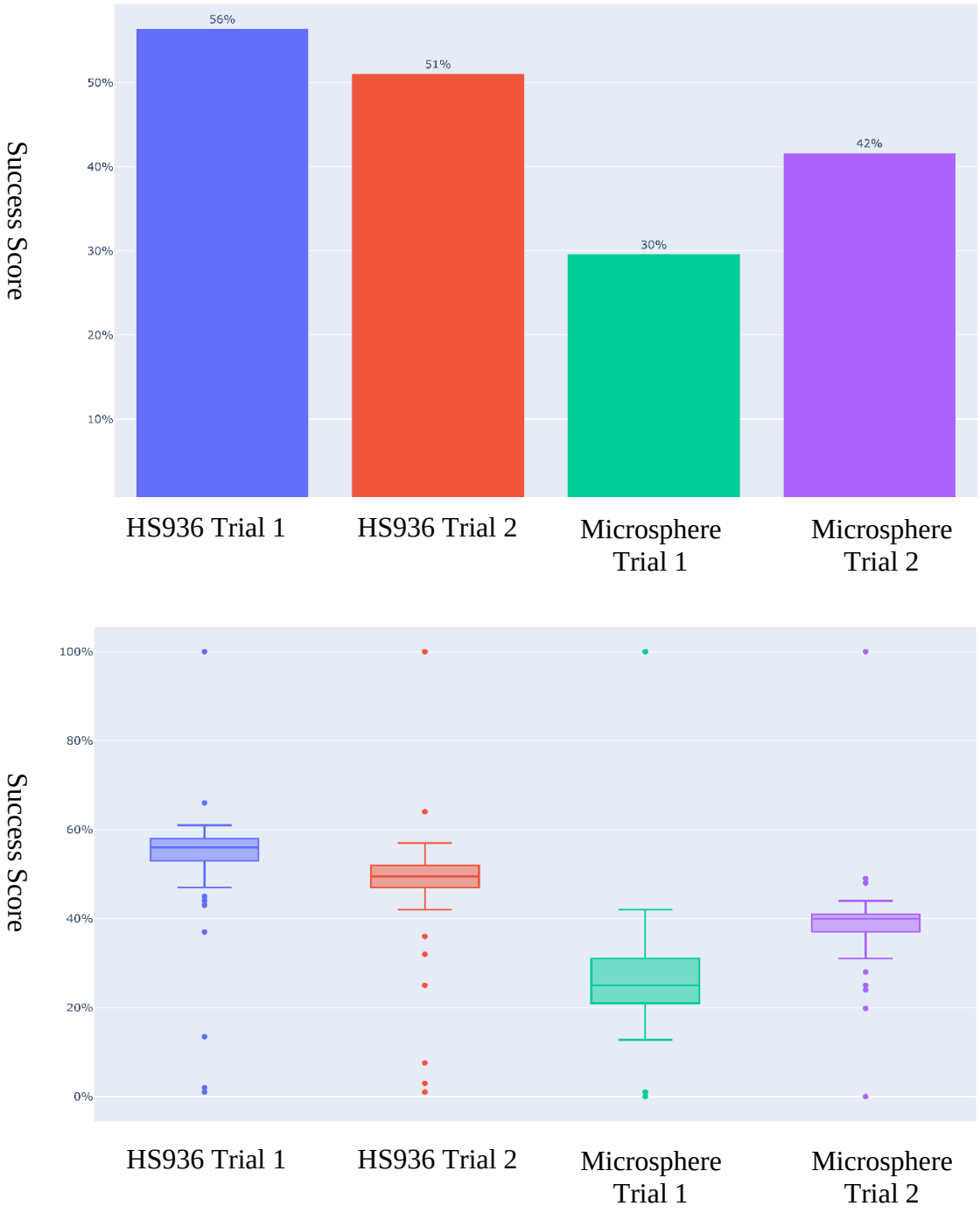

Fig 19. Overall model scoring for 100 DNN autoencoder. No trail scored over 60% success in classification. Model sore distribution validates average score calculation.

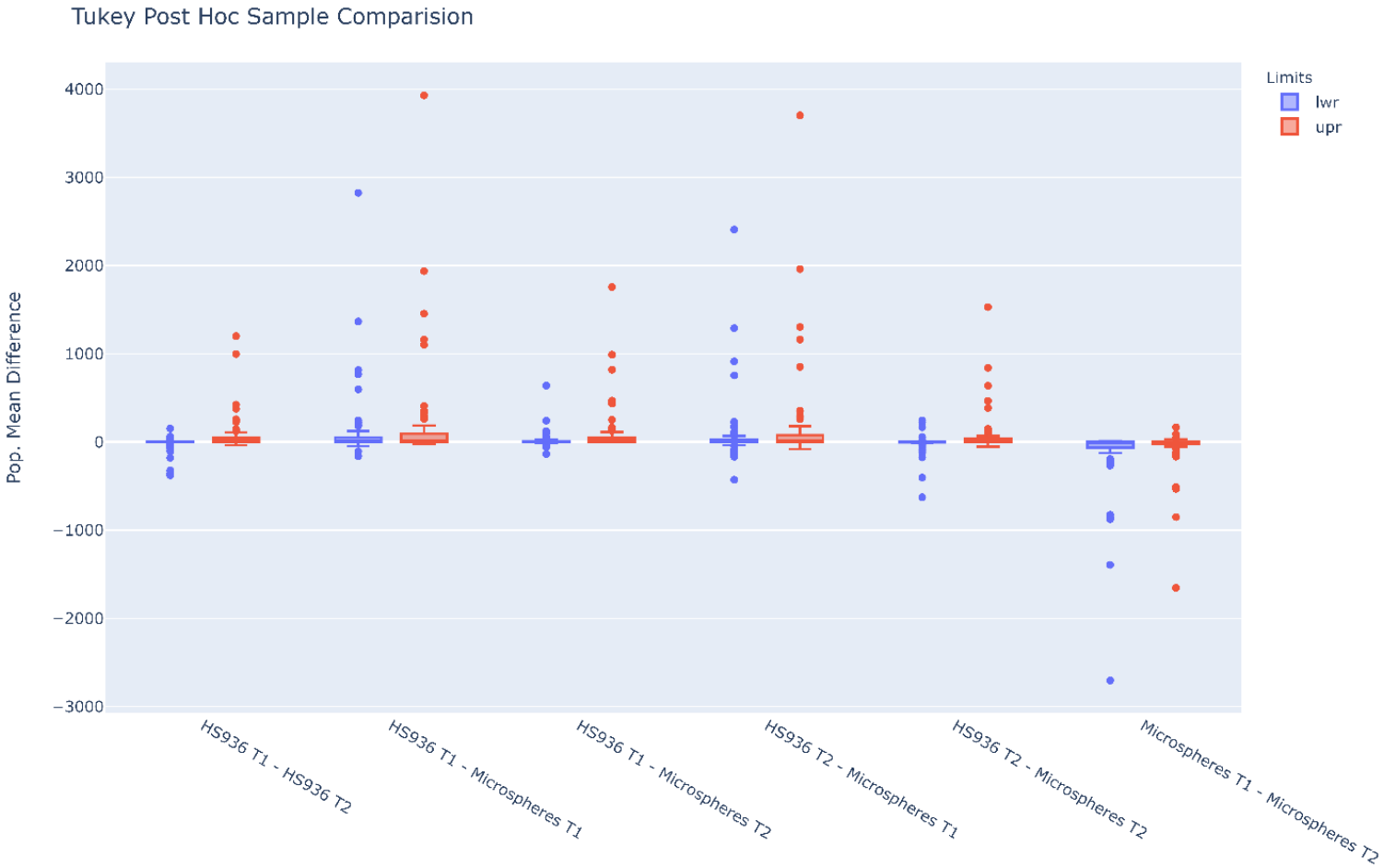

Fig 20. Tukey Post Hoc analysis discerns the difference between populations. Population close to zero would suggest populations with low mean difference, allowing for the conclusion that the populations are significantly similar.

All model Post Hoc analysis for DNN autoencoders display populations with confidence internals including zero (Fig. 20). This suggests high similarity within all populations and no statistical significance. Without significance in population means, feature mapping would not be robust enough to discern any valuable information. Selectivity was tested within models to discern whether any significant differencing within population was obscured.

Top 20 models based on HS936 performed much better than the overall model success calculations. Distribution analysis of model success confirms overall calculation. It is important to note that variation analysis depicts models that were completely successful in classifying signals (Fig. 21). Deeper investigation showed these models to be overfit, all points were reduced to a coordinate pair of (0,0), producing no valuable feature data.

Excluding these overfit models, Post Hoc analysis of top 20 non-overfit models depicted populations centered highly around zero population mean difference (Fig 21). This would suggest no valuable information can be gained from feature mapping. Plotting the most successful autoencoder with centroids included shows that the model was unable to distinguish any difference between trails (Fig. 22). This suggests an insufficient amount of data within training population or insufficient feature differencing within signals themselves.

Fig 21. Variation reaching 100% success on all classification suggests overtraining within the randomized models. Excluding these models in Post Hoc analysis suggests significantly similar populations.

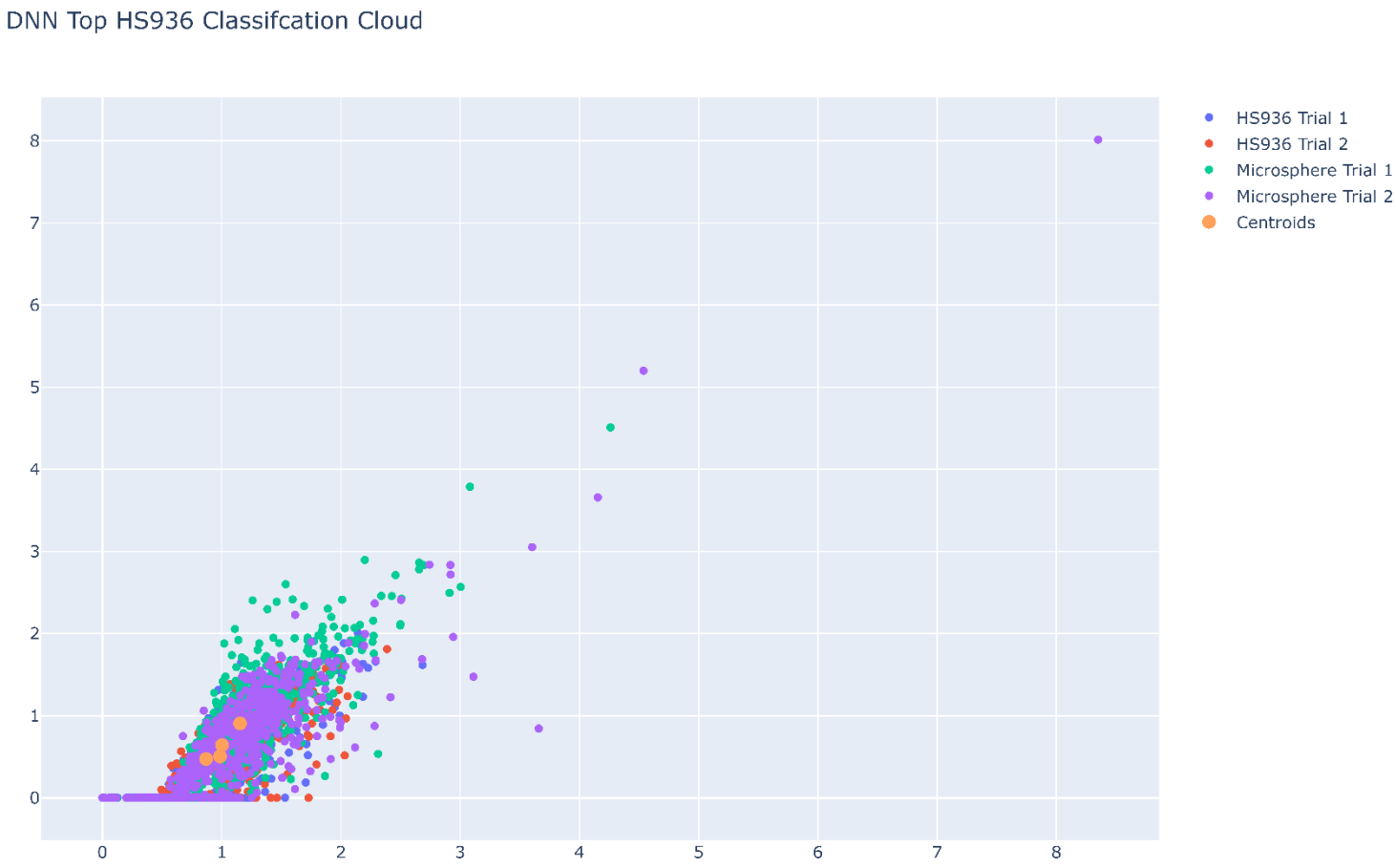

Fig 22. Feature map produced by the highest scoring HS936 model. All populations overlap displaying no significant feature separation.

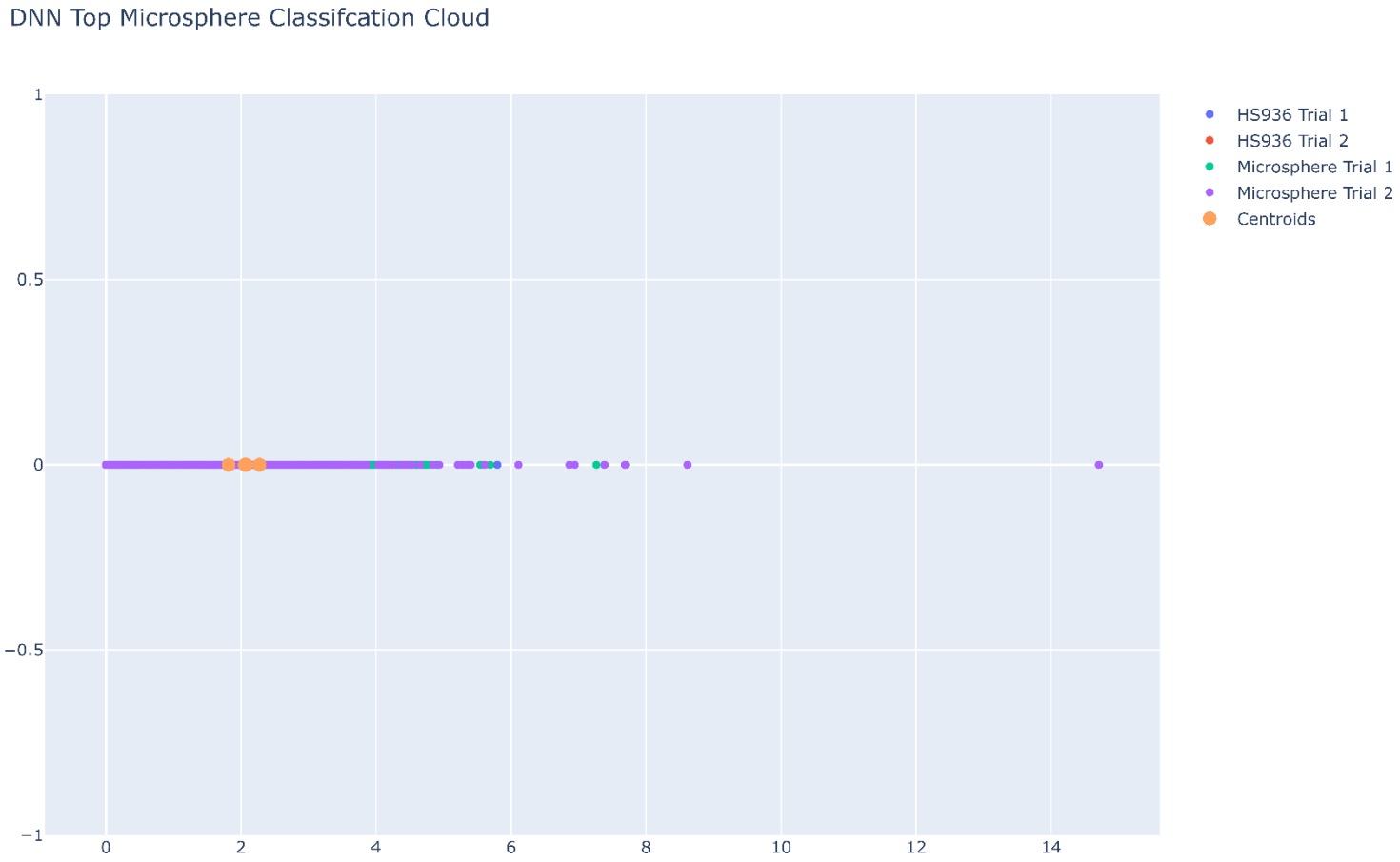

Fig 23. Highest scoring microsphere model trained with insufficient feature data resulting in overfitting.

Evaluation of top 20 models based on microsphere classification were consistent with the observation of insufficient difference in training data population. Variation analysis within models again showed presence of overfitting. Post Hoc analysis of non-overfit models displayed similar populations that would create statistically insignificant feature maps. In the case of the highest performing autoencoder, the dimensionally was reduce to a single point rather than a pair (Fig. 23). This can occur in overfit models or models trained on data with insignificance feature differencing, causing one of the outputs in the coordinate pair to be pulled to zero.

CNN Autoencoder

CNN autoencoders were chosen to assess the possibility of a feature map produced from an entire event signal. Similar to the DNN autoencoder, CNN autoencoders dimensionally reduced their inputs to a ReLU activated coordinate pair. Inputs of the autoencoder were smoothed and scaled for the same reasoning behind CNN classification. Overall, success scores out of 100 randomized models were more successful than DNN autoencoders but not as successful compared to strict classification. Variation of success scores verifies overall model scoring (Fig. 24). Post Hoc analysis of autoencoder populations depicts populations based around zero. This causes the assumption that autoencoder populations were insignificantly different and would be unable to produced valid feature maps. To account for selectivity the top 20 scoring models were analyzed.

The 20 highest scoring models for HS936 display great selectivity for the HS936 signal. Less than 20% of the time, microsphere signals were correctly classified. Post Hoc analysis of autoencoder populations displays difference means including zero. However, the variance within the means suggests the possibility of significant population difference

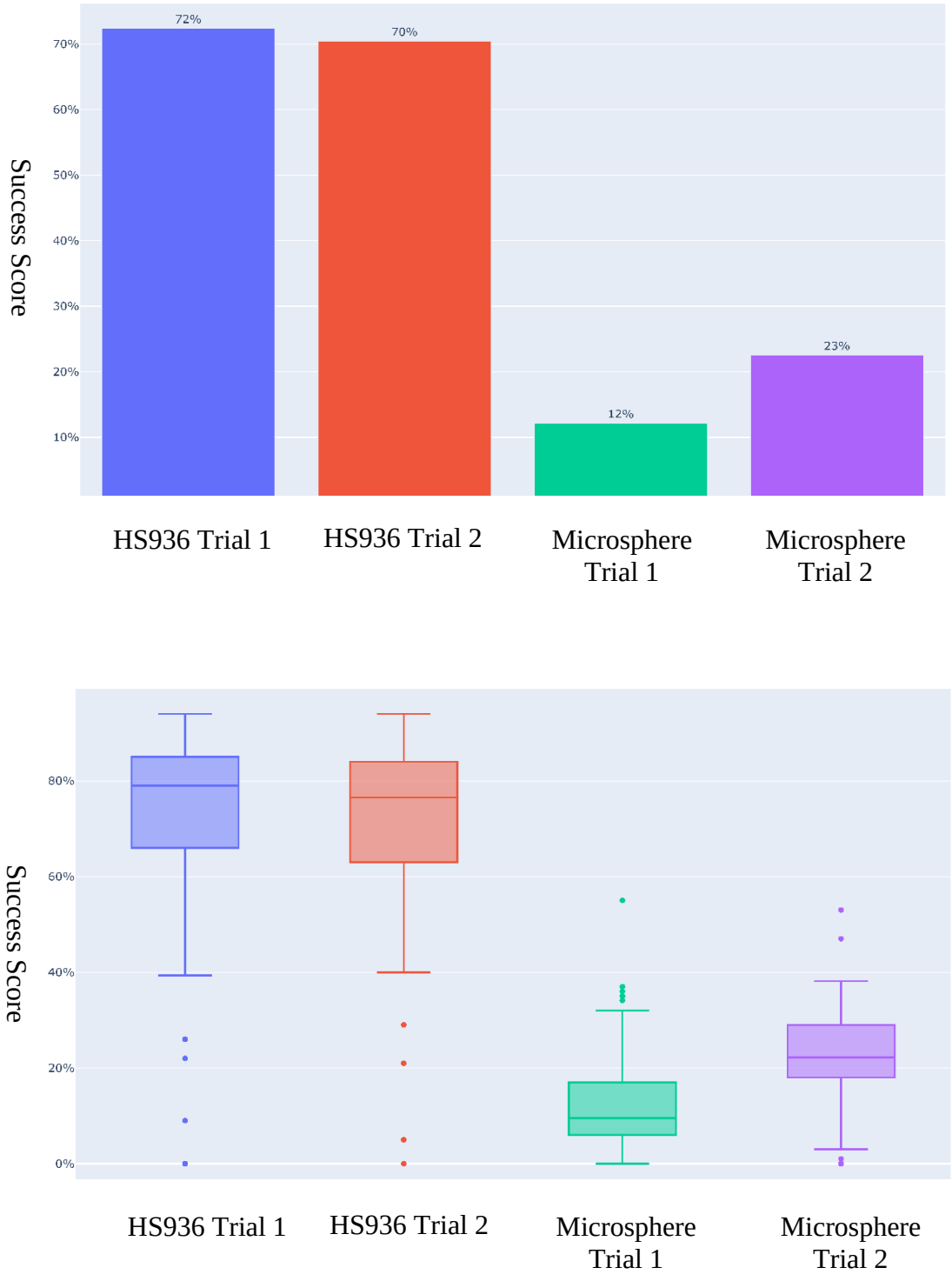

Fig 24. Success scores for 100 randomized CNN autoencoders. Distribution of the scores validates average success calculation.

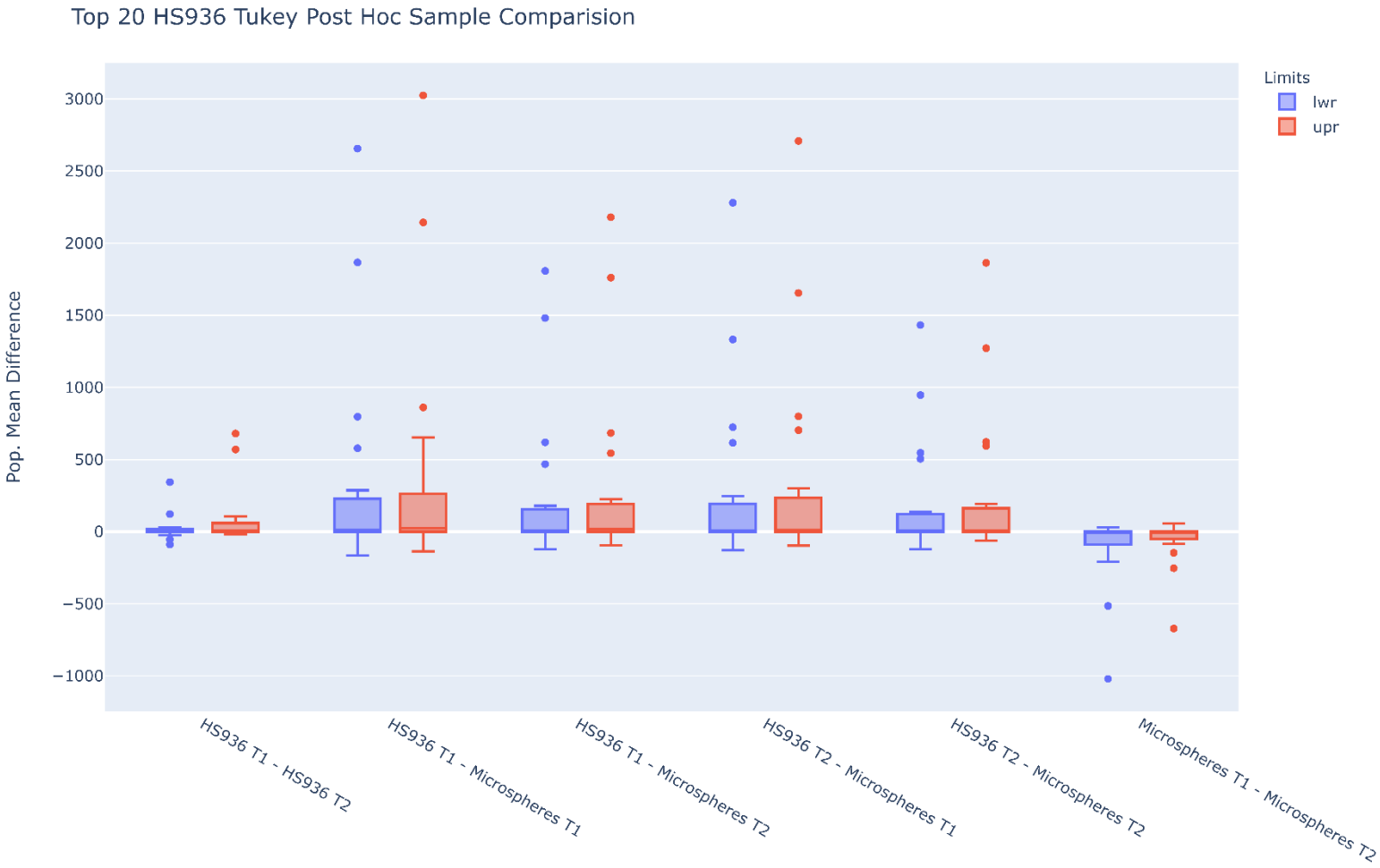

Fig 24. Variation in Post Hoc analysis suggests partial success in feature mapping in some models

on some of the models (Fig. 24). As expected, differencing in HS936 and microsphere trials appears to be unchanged. This suggests that features are relevant to particle and not particle concentration, which differs from evidence found in classification models.

Graphing the most successful HS936 autoencoder with centroids depicts a somewhat crude feature map (Fig. 25). HS936 and microsphere centroids are grouped closer together suggesting similarity in signal interpretation. Distinct groupings can be discerned suggesting prevalence of a fairly strong feature within event signals. Overlap within the populations points towards something obscuring the full weight of the featuring being leveraged. As the pull was reduced by an abundance of data in classification; it is possible that a feature exists within the event signals but is clouded by an excess of featureless data.

Top 20 highest scoring microsphere autoencoder again displayed selectivity for HS936 signal. Success scores for these models were dramatically lower in all categories. Variation within model scores supports overall scoring. Post Hoc analysis depicts populations focused around zero suggesting highly similar populations. Though variation is evident it is much lower than variation observed in HS936 based models. Coordinate cloud of most successful model shows almost completely overlapping populations. Again, microsphere-based models performed poorly when compared to HS936 based models.

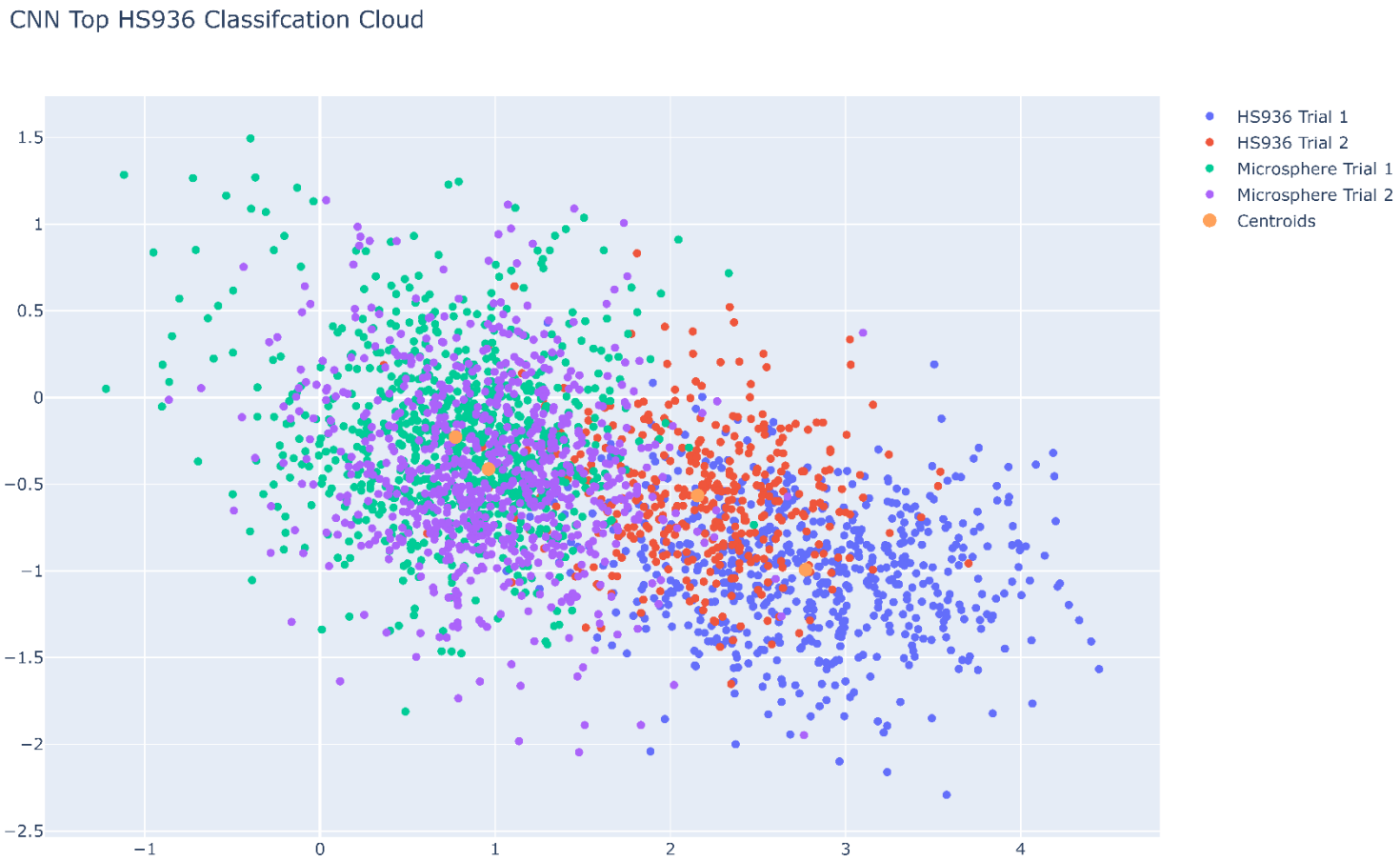

Fig 25. Highest scoring microsphere model trained with insufficient feature data resulting in overfitting.

Though classification tests showed high success in classifying event-based signals and suggest prominent features within event signals the autoencoders were unable to produce robust feature maps. The reasoning for this lies within the neural networks ability to perform non-parametric classification. CNN autoencoders focused on HS936 signal bases were able to produce weak feature maps. However, strength for these maps were determined by parametric differencing. Euclidean distancing is a linear approximation of class, meaning the feature produced by the autoencoder were parametrically weak. Non-linear classification of the same points could produce a much more efficient classification. This, however, is unhelpful when trying to produce a feature map due to its parametric nature.

Chapter 6

Results of Fundamental Analysis

Parabolic Extension

The data gained from neural network training, specifically autoencoder constructions, suggest waveforms contain fundamental components. These components separate signals of different particle compositions but maintain similarity between differing sample concentration of different cells. Parabolic extension was leveraged to increase signal fidelity while maintaining realistic acoustic prorogation. Prior to extension all samples are minimally smoothed and squared. This is to reduced digitization and base AC signal oscillation. Event signals are then parabolically extended in both the sample and signal direction (Fig. 26). Complete parabolic extension explanation is located in the supplemental materials.

Signals are then reduced in the opposite dimension in which extension occurred. This is done to obtain a profile image of the event peak signal. Again, this signal is assumed to be representative of the event. During mass spectrometry analysis, a mass peak resolution is obtained. This is to differentiate signals of different mass charge ratios, allowing for finer classification of data. Similarly, acoustic signals can be seen as related to mass spectrometry peak readings. However, acoustic readings are subject to much more noise and signal crowding due to their time dimension dependence. This allows us to assume a perfect propagation wave. Without noise and surrounding signals, a perfect wave could be a single parabola at the midpoint of its wave propagation. This would mean on a flattened profile of the wave two parabolas can be ascertained and classified (Fig. 27).

Assuming thermoacoustic response is dependent on more than just wave strength, a peak resolution could be used as a classification marker similar to mass spectrometry.

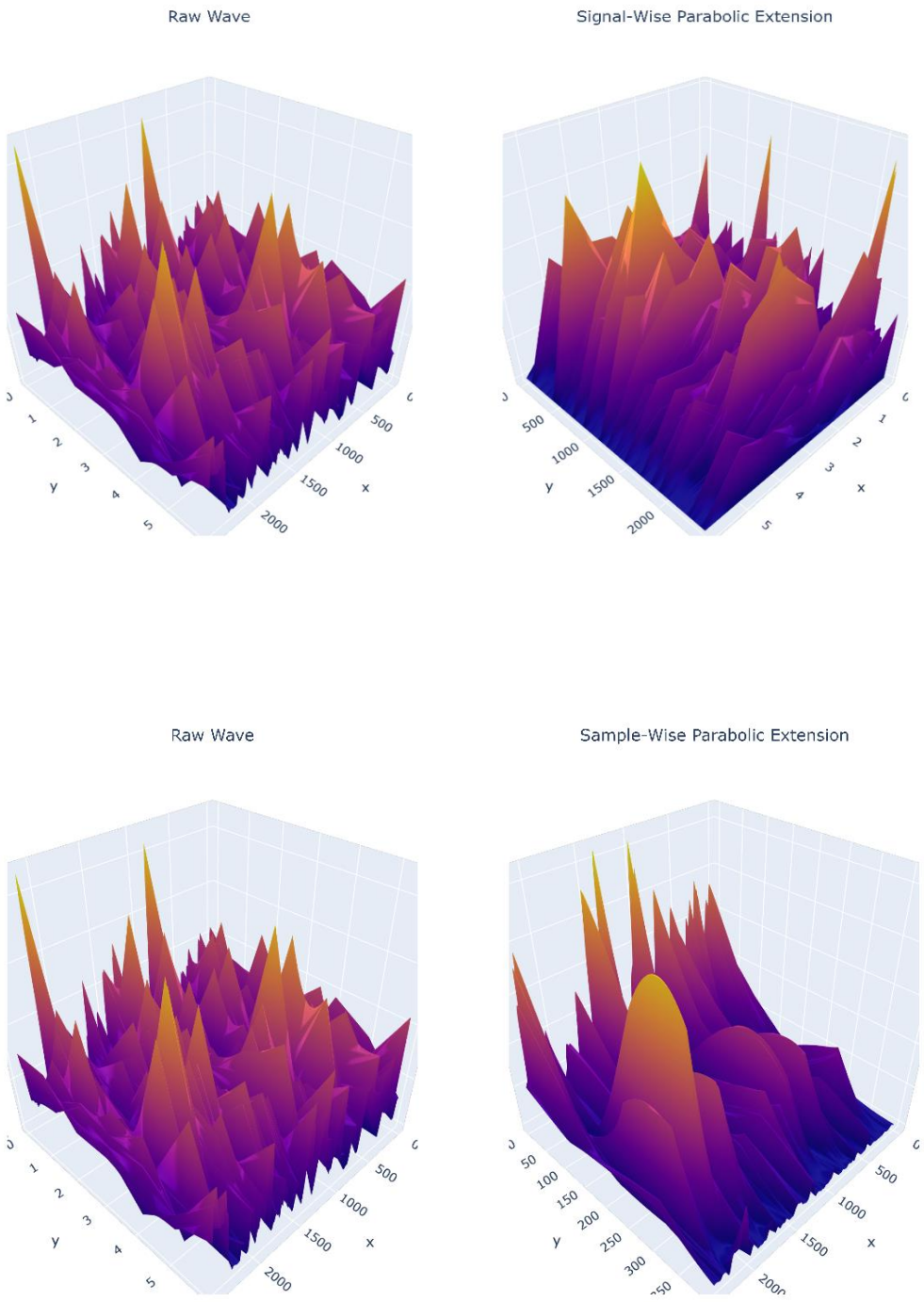

Fig 26. Parabolic extension in both sample and signal direction. Extension seeks to increase data points for analysis while maintaining laminar wave nature.

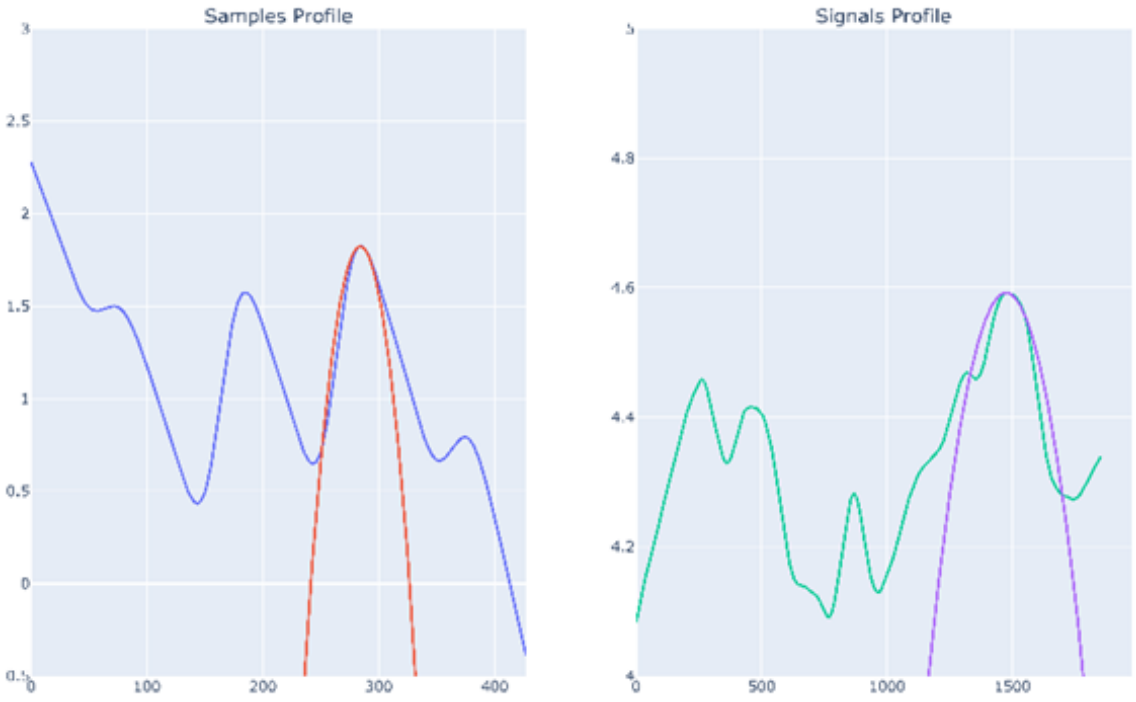

Fig 27. Image of wave profiles from both sample and signal dimensions. These profiles have been extended and fit with parabolas to mimic "perfect" wave propagation. Ideal waveforms resemble mass spectrometry readings, imaged above.

Fitting parabolas to the highest peak in each profile, by averaging the surrounding parabolic slopes using the peak as the vertex, we can assume an undisturbed acoustic wave mid propagation. We can obtain our peak resolution by calculating distance between the wave at selected fractions of the total wave power. Resolution power can be calculated by dividing the difference distancing by total wave amplitude. For sake of investigation three power fractions were tested (25%, 50%, 75%) and area calculated above the fraction lines was calculated. Area was included in the investigation to capture the potential of a significant integral in wave propagation in the absence of other significant wave characteristics.

Using analysis of variance (AOV) statistical analysis on the interaction of all novel statistics, many were found to be highly significant in discerning particle type from waveform. Full AOV tables are found in the supplemental materials. Some of the statistics

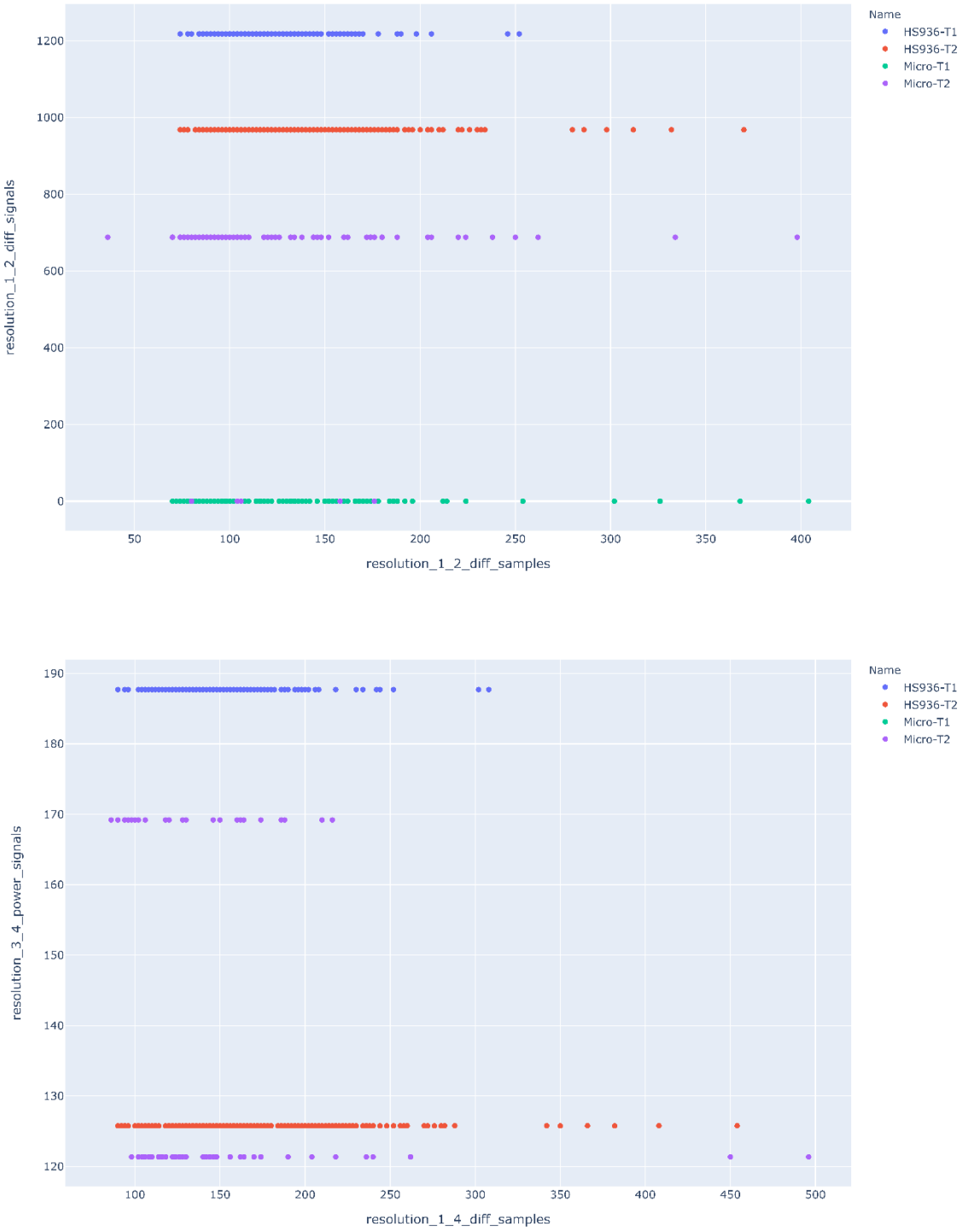

Fig 28. Some feature interaction scored highly in classification of waveforms. Depicted below are interaction plots for 50% wave difference and 50% signal AUC vs 75% sample difference distance.

were highly selective in their classification (Fig. 28). Feature isolation can further improve neural network success. DNN classification models were again run in the same randomized schema. Inputs were scaled within their own feature populations and outputs were tied again to one and zero respectively. Overall model scores were much higher than original single wave classification. Variation analysis confirmed overall scoring. Inspection of selectivity displayed minimal pull on classified signals.

When running autoencoder trials, many of the models were prone to overfitting. As a result, no meaningful data could be derived from autoencoder exploration. Manual development and tuning of autoencoders revealed unique morphology within the resulting plots. Specifically, all of the plots lacked exploded traces of the original microsphere trial. Training data was consistent with methodology suggesting models consistently chose microspheres as comparison base other samples. Morphology of the resulting plots appears non-linear suggesting deeper set features within the computed novel features.

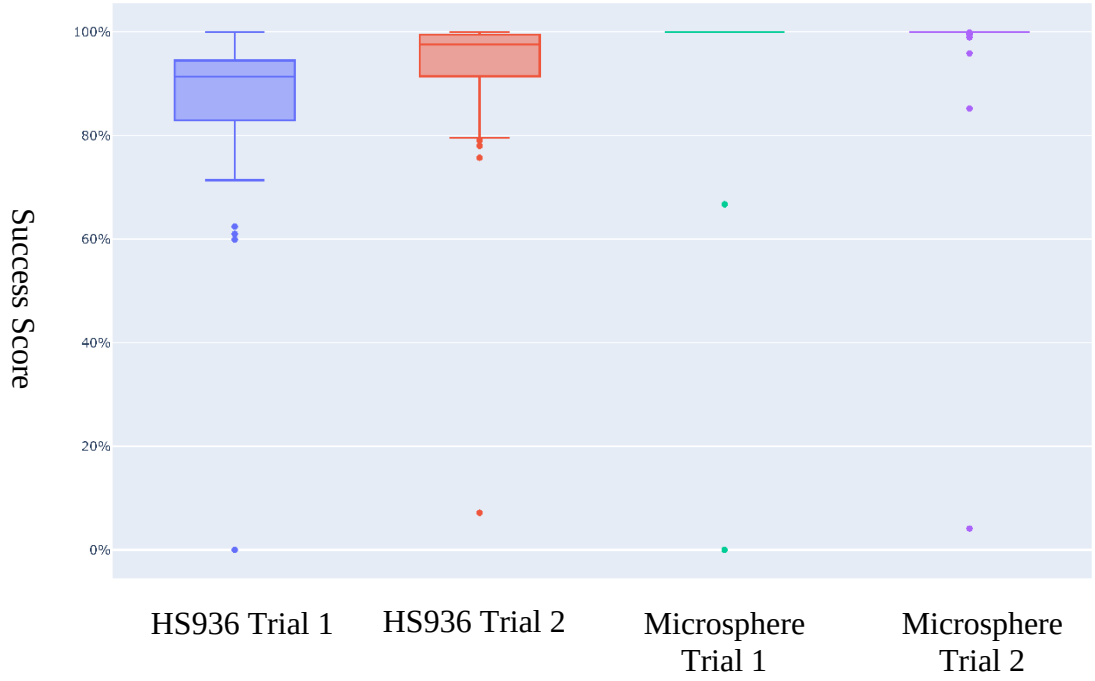

Fig 29. Success distribution for 100 DNN classification models using novel features as inputs.

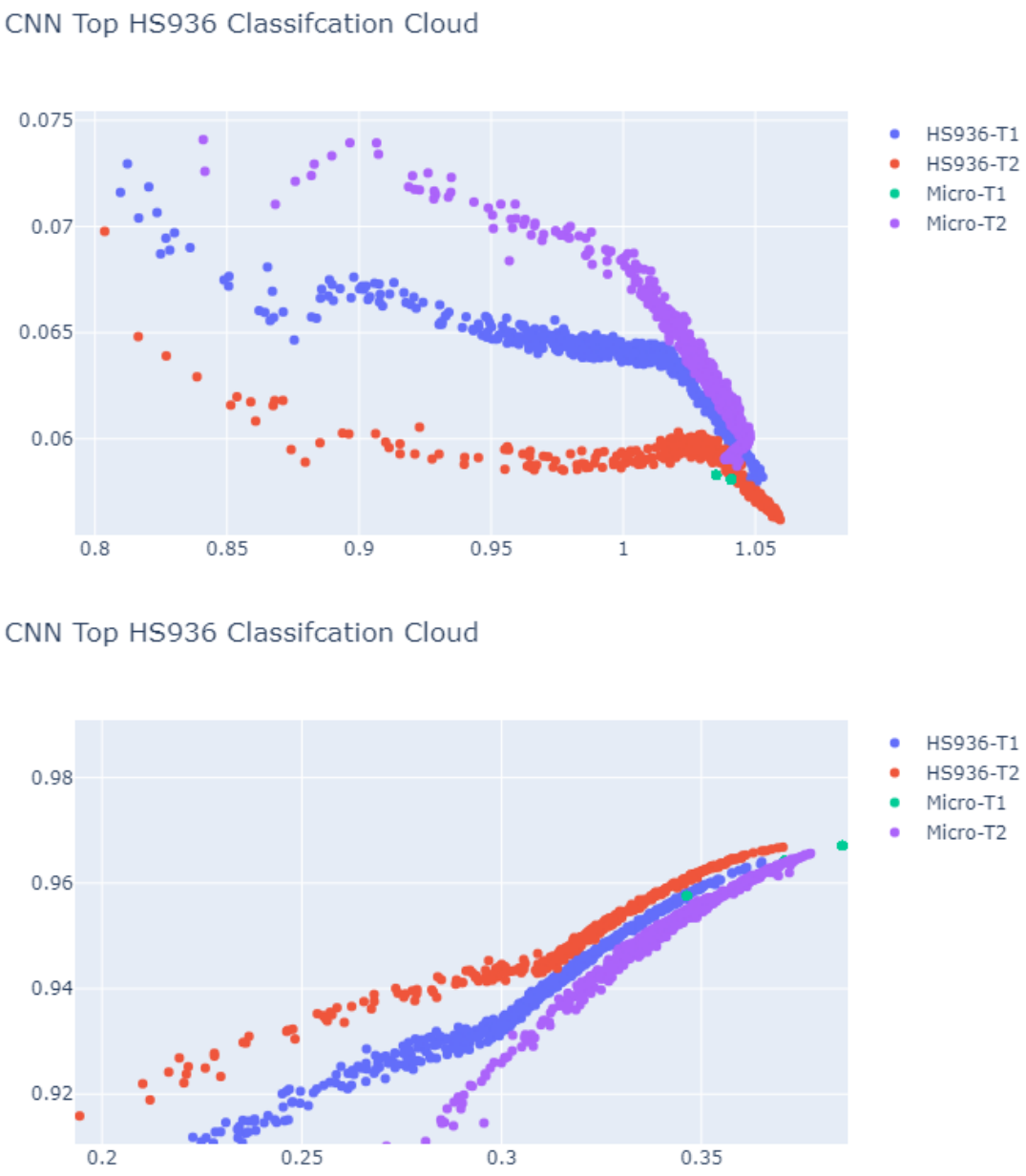

Fig 30. Autoencoders produced by novel feature training

Shark Fins

During fundamental analysis and morphology exploration it was found that after parabolic extension in the samples direction and multiple smoothing and squaring cycles, event signals take on a specific morphology. Peak signals and surrounding waves appear as “shark fins” (Fig. 31). This novel characteristic appears specific to wave morphology. Under the same processing HS936 events appear to take on a sharper fin tips than microsphere signals (Fig. 32). Whether this speaks to the power behind the acoustic wave or the amplification afforded by particle composition is undetermined. Another phenomenon that arises is the idea of “schooling”. The construction of the flow system does not allow for intended single cell testing. Testing is not designed currently for characterizing single cell response but rather clinical diagnosis. This means that multiple particles can be present within the laser’s beam and multiple acoustic waves are created.

Focus specifically on the following figure of a microsphere detection event. The y-axis represents the signals of a sample while the x-axis represents multiple samples of the event. The peak sample is present in the middle of the event. However, there are surrounding waveforms. Detection rates are dramatically lower than ground truth cell counts. Again, this speaks to the purpose of the system. The system is for clinical diagnosis not particle characterization. Multiple cells are allowed within the detection volume at a given time. The schooling observed are the surrounding particles releasing energy.

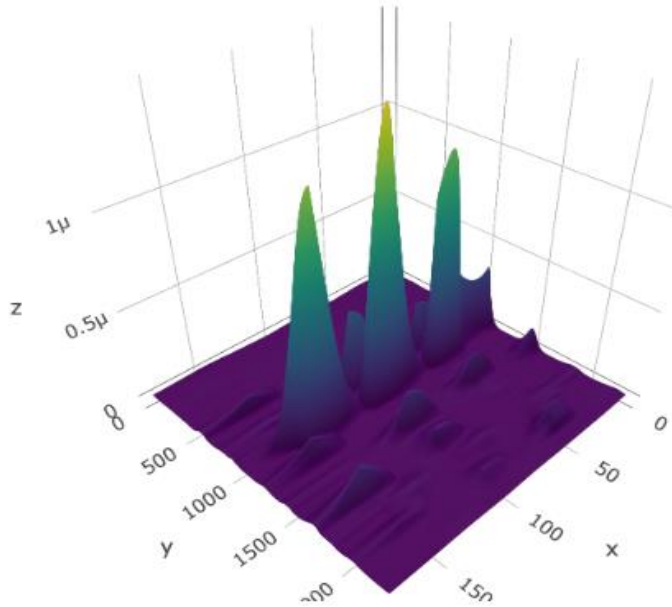

Fig 31. Microsphere event signal shark fin morphology.

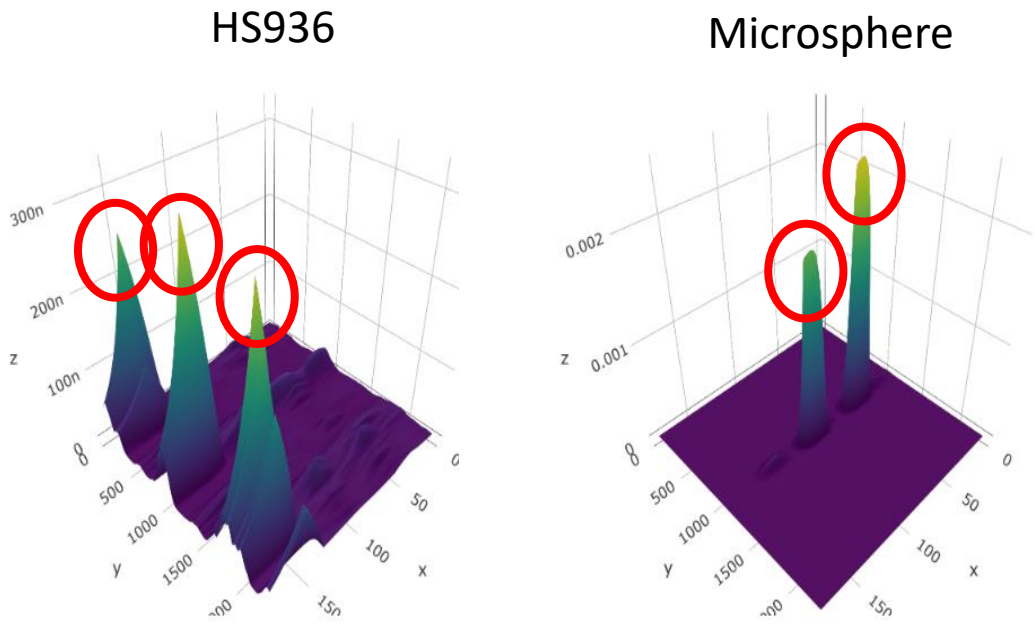

Fig 32. Difference in tip shape between HS936 and Microsphere detections

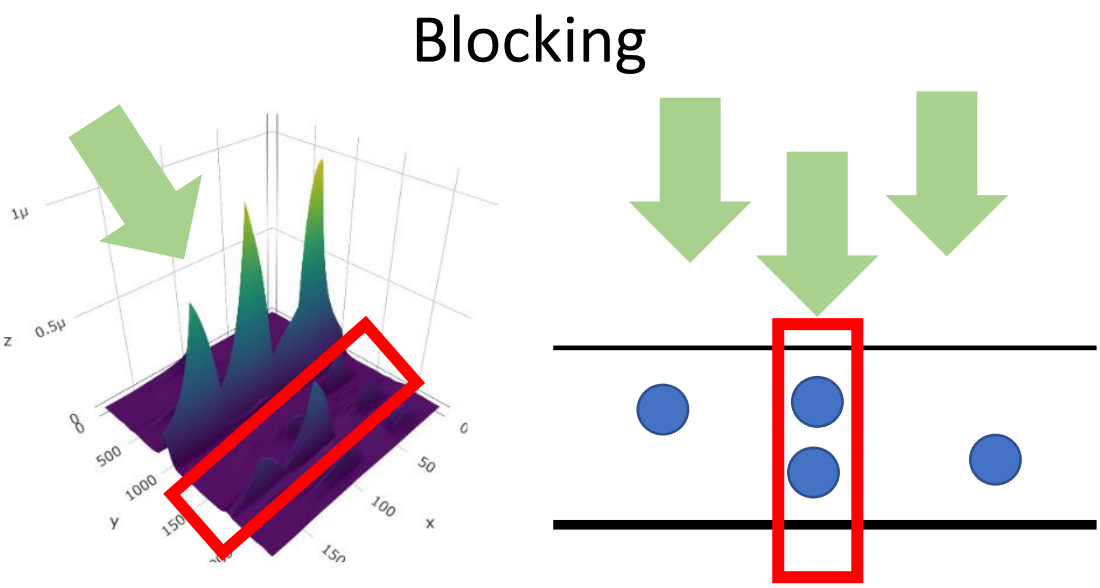

Fig 33. Blocking present in sample and visualized through recreation

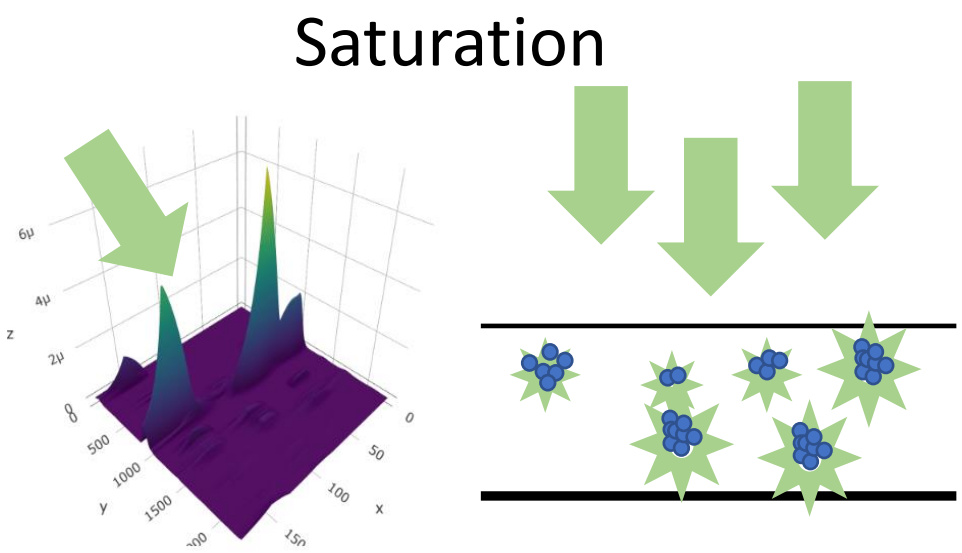

Fig 34. Saturation present in sample and visualized through recreation

Multiple assumption must be made to explain schooling behavior. Blocking, for example, must occur within detection events. The probability of a single particle blocking another particle is extremely low, however, when picturing a saturated detection volume energy is rationed to the particles closest to the beam side of the quartz tube. Which would mean waveforms along the signal axis, y-axis, would block later signals. This can be seen in the small wave behind the event peak wave. Energy is more readily consumed by closer particles resulting in a smaller wave emitted from blocked particles (Fig. 33).

However, there is a secondary wave in front of the peak wave, slightly obscured from view. Blocking would assume this wave receives the most energy and should have the stronger response. This gives evidence that wave energy is determined by a factor stronger than blocking, saturation. Though it is possible for a single cell to be detected in the system, when multiple particles are present multiple signals must be lost to saturation of transducer, only the strongest waves would be observed. Assuming every particles response is similar to thermal input, every waveform would be similar and lost due to saturation. Therefore, energy from multiple waves must combine and would be represented in a single detection waveform (Fig. 34). This phenomenon can be compared to a pixel in an image. A pixel is a summation of the light accepted by the sensor. Multiple photons are accepted by a single sensor, the higher the photon count the brighter the pixel in the final image. Multiple acoustic waves are combined within waveforms present in a detection event due to summation by the transducer.

Using the saturation assumption, it is possible to reconstruct the particle count from the number of waveforms observed. Without knowing the specific response of a single particle, the smallest waveform within the detection event must be assumed to be a single

particle. Peaks are captured in both signal and sample event directions. Heights of the peaks are recorded and cataloged in a data frame. Both data frames are merged by their heights with 2 decimal precision. Unmerged columns are discarded, and remaining heights are assumed to be peaks. All heights are divided by the minimal height detected in the event and summed. The reconstructed detection counts highly correlate with original sample concentration (Fig. 35).

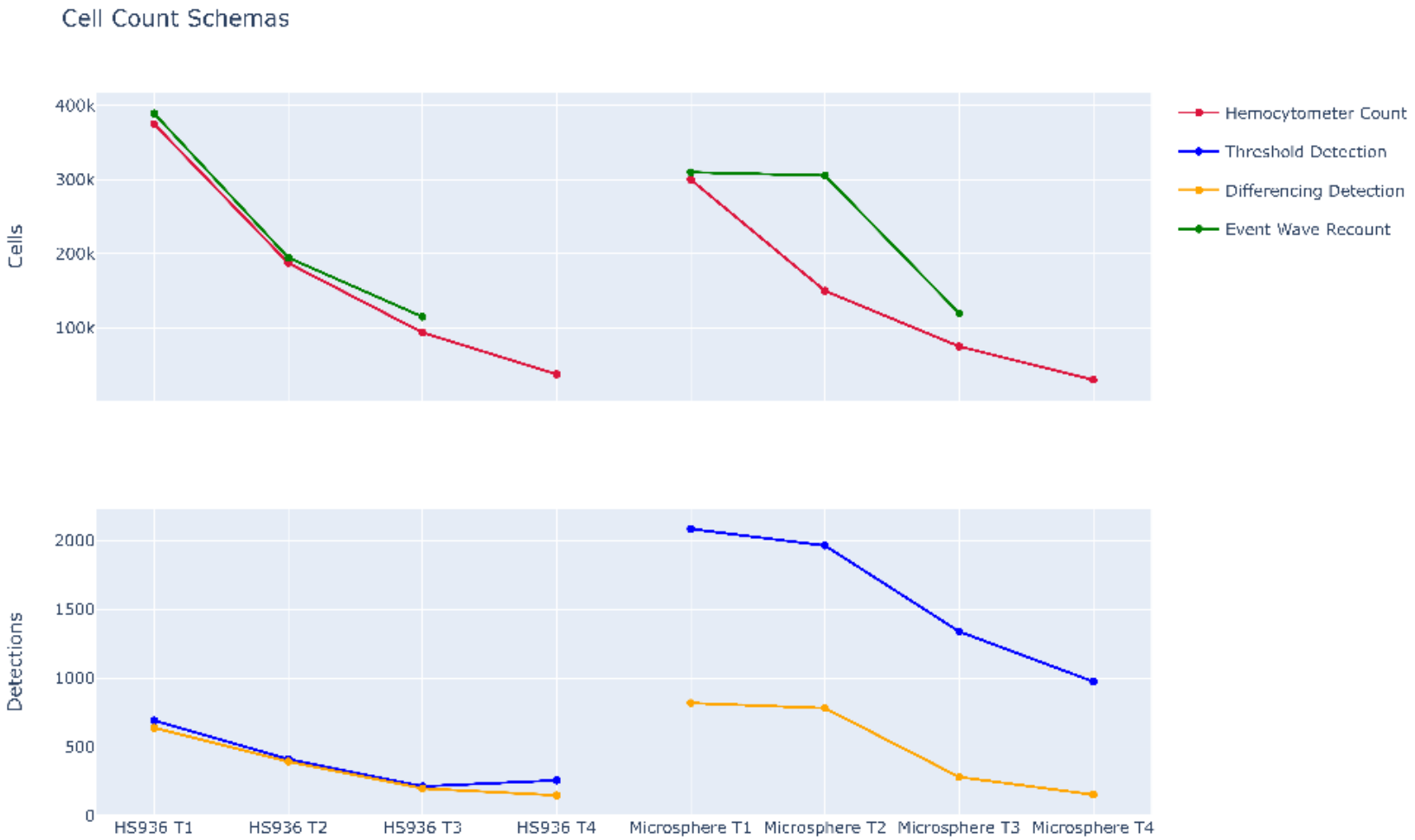

Fig 35. Actual sample concentrations with reconstructed counts and cell detection counts using both detection methodologies. X-axis is share between graphs.

Chapter 7

Post Analysis Summary

Classification Investigation Summary

Both DNN and CNN network structures were leveraged to assess the possibility of wave classification. DNN networks focus on peak wave classification and were unsuccessful in producing a robust solution. Selectivity was observed within model training and suggested choosing of a base signal for differencing. Pull was observed in DNN models suggesting features exist within waves by are not found strongly enough in the peak wave for robust classification.

CNN models were used to assess the possibility of classification of event signals. Event signals are composing of 7 samples surrounding a peak wave which was the basis of original detection. The assumption was wave propagation is better observed when including a time dimensions to the detection event. CNN classification was highly successful and able to perform robust classification. Selectivity was again viewed in model training and signals were chosen as a base for differencing. Pull was again observed but to a lesser extent in CNN models. Pull is possibly lessened by the amount of overall data points used in the model's input. Due to CNN success, evidence suggests wave features more highly present in event data than peak wave data.

Autoencoder Investigation Summary

Autoencoders were utilized to access the possibility of the creation of feature maps based on particle thermoacoustic response. Success of autoencoders was limited and markedly less than that of pure classification. DNN autoencoders were again trained on single peak waves which were assumed representative of the signal. Success was scored

by classification of particles using centroid distancing. Resulting point clouds were unhelpful in creating any form of feature map, data was too correlated. Tukey post hoc analysis confirmed visual assumption of populations which were too similar for feature mapping.

CNN autoencoders again performed markedly better than DNN autoencoders but were still unsuccessful in feature map creation. CNN autoencoders scored much lower than CNN classification networks. Resulting point clouds were much stronger candidates for feature mapping but post hoc analysis revealed populations too similar for robust feature mapping. Differing success between classification and autoencoding structures was attributed to non-paramedic classification. Feature maps and centroid distancing are parametric tools which would serve poorly in classifying populations without parametric distributions. Network abilities to mutate to task allow for greater ability for non-parametric separation.

Waveform Reconstruction Summary

Exploratory inspection of event wave forms was conducted to deduce the presences of underlying features that could determine classification. Fidelity of waveforms were increased through parabolic extension. Parabolic extension was chosen to best represent the natural form of a laminar acoustic wave propagation. Extension was conducted separately on both dimension and resulting profiles were compiled from extended waveforms. Profiles were reminiscent of mass spectrometry readings high in noise and low in signal strength. This prompted the methodology to treat the acoustic wave similar to mass spectrometry readings.

Surrounding data was assumed to obscure pure acoustic waveforms. A parabola was fit to the highest peak in both profiles with the maximum point as the vertex. Slopes

extended limited distance beyond the maximum point and were averaged to reconstruct the assumed pure waveform. Novel features were extracted from the pure waveform and included peak resolution difference, power, and summed area.

Novel Feature Classification Summary

Novel features were analyzed using AOV statistical testing. Interactions of many of the features proved to be highly determinate in the classification of their parent wave. Whether this is representative of other particle types or higher volume of test data should be determined in a later study. By creating novel features, confounding factors would be removed from detection data and further neural network exploration could be conducted.

DNN classification structures were highly successful when trained on novel feature set. Selectivity of features was not performed, and it is unknown whether some of the resulting features or their interactions were confounding to overall success, this should be further investigated. DNN autoencoders were prone to overfitting and produced no valuable feature map data. Whether this is due to confounding features is unknown and should be investigated. Present assumption is that wave features are inherently non-parametric and cannot be reduced into a feature map. Some point clouds show promise for feature mapping based off linear or curved line fitting. Whether these grouping are based on an underlying thermoacoustic characteristic should be investigated. Separation of similar particle types suggests whatever resulting characteristic is also scaled with cell concentration in some manner.

Shark Fin Investigation Summary

“Shark fin” structures were noted during morphology investigation. Under repeated cycles of event smoothing and squaring, detections appear as structures resembling shark

fins protruding from water. Shark fin size appears to correlate with detection strength and represent particle positioning within detection volume during events. Multiple phenomena arose when studying shark fin morphology termed “blocking” and “saturation”. Blocking occurs when particles closer to beam side of the detection volume receive and decrease overall energy as it passes through detection volume. This can be seen in smaller waves that appear to be overshadowed by larger waveforms. Saturation is the phenomena that explains greater wave strength when overall particle response should be uniform. HS936 thermoacoustic response should vary with the amount of produced pigment. However, microsphere shark fins vary in the same way suggesting a different explanation. The transducer used is focused and lower waveforms surrounding peak detections could be explained as signals outside of focus. However, transducer focus would be static and peak detections move throughout detection events. Smaller signals also surround peak signals in a pattern termed “schooling”. Saturation explains this variation in wave strength by attributing it to the combination of multiple more uniform particle responses. Due to saturation of samples the transducer is not capable of differentiating overlapping waveforms and therefore sums them.

Using the saturation phenomenon assumption, a recalculation of total cell detection can be conducted on peaks that were not representative of the detection. Overall, signal detection is a poor representation of overall sample concentration, several orders of magnitude less than ground truth. By detecting the peaks within a event, and assuming any variation in height is the summation of smaller peaks, one can back calculate total particle concentration within a sample’s detection set.

Chapter 9

Conclusions

Photoacoustic flow cytometry is a technique founded off the principles of inherit particle thermoacoustic characteristics. The system used in this experimentation was designed for clinical diagnosis of circulating tumor cells. By exciting pigmented cells, such as melanoma, an acoustic waveform can be produced, collected, and serve as evidence for cell existence. Great promise has been shown in clinical applications of this technology. The experimentation explained in this paper sought to analyze detection signals for the ability to further classify detections, increasing clinical viability. Detections were expanded from a single waveform to a time dependent event. Events were reconstructed for visual analysis and allowed for creation of multiple morphological phenomena. Neural networks were leveraged as the primary mode of morphology exploration and assessment of potential feature mapping. Resulting fundamental investigation confirmed neural network evidence. Waveform morphology is of non-parametric distribution. Neural networks, specifically Convolutional Neural Networks, are equipped for robust signal classification, but feature mapping was not viable for the techniques used in this research.

Supplemental Materials

Unfit models were discarded and randomized again. Overfit models were protected against with early stopping. No significant change in training loss caused model to be discarded and randomized again

DNN Classification Model Structure

Input Layer
Dense Layer Node Length Range 1-4000
Dense Layer Node Length Range 1-500 20% Chance of Occurrence (CO)
Dense Layer Node Length Range 1-500 40% CO
Dense Layer Node Length Range 1-500 20% CO
Dropout Layer 0-50% Rate 40% CO
Dense Layer Node Length Range 1-500 20% CO
Dropout Layer 0-50% Rate 40% CO
Dense Layer Node Length Range 1-500 20% CO
Dense Layer Node Length Range 1-500 40% CO
Dense Layer Node Length 1

Epoch Range 20-50
Batch Size 26-56
Model Trained on HS936 375000 cells/mL/ Microspheres 300000 cells/mL

DNN Autoencoder Model Structure

Input Layer
Dense Layer Node Length Range 1-512
Dense Layer Node Length Range 1-512 20% Chance of Occurrence (CO)
Dense Layer Node Length Range 1-512 40% CO
Dropout Layer 0-50% Rate 40% CO
Dense Layer Node Length Range 1-126 20% CO
Dense Layer Node Length 2 **Encoder Layer**
Dense Layer Node Length Range 1-126 20% CO
Dropout Layer 0-50% Rate 40% CO
Dense Layer Node Length Range 1-512 20% CO
Dense Layer Node Length Range 1-512 40% CO
Dense Layer Node Length **Input Length**

Epoch Range 20-50
Batch Size 26-256
Model Trained on HS936 375000 cells/mL/ Microspheres 300000 cells/mL

CNN Autoencoder Model Structure

Input Layer
Convolution Layer Kernel [1-2,100-250] Node Length Range 1-32
Convolution Layer Kernel [1-2,100-250] Node Length Range 1-32 40% CO
Pooling Layer Kernel [1,2-4] 40% CO
Convolution Layer Kernel [1-2,100-250] Node Length Range 1-32 40% CO
Convolution Layer Kernel [1-2,100-250] Node Length Range 1-32 40% CO
Pooling Layer Kernel [1,2-4] 40% CO
Convolution Layer Kernel [1-2,100-250] Node Length Range 1-32 40% CO
Convolution Layer Kernel [1-2,100-250] Node Length Range 1-32 40% CO
Pooling Layer Kernel [1,2-4] 40% CO

Flatten Layer
Dense Layer Node Length Range 250-500
Dense Layer Node Length Range 1

Epoch Range 20-50
Batch Size 26-256
Model Trained on HS936 375000 cells/mL/ Microspheres 300000 cells/mL

CNN Autoencoder Model Structure

Input Layer
Convolution Layer Kernel [1-2,100-250] Node Length Range 1-32
Convolution Layer Kernel [1-2,100-250] Node Length Range 1-32 40% CO
Pooling Layer Kernel [1,2-4] 40% CO
Convolution Layer Kernel [1-2,100-250] Node Length Range 1-32 40% CO
Convolution Layer Kernel [1-2,100-250] Node Length Range 1-32 40% CO
Pooling Layer Kernel [1,2-4] 40% CO
Flatten Layer
Dense Layer Node Length Range 250-500
Dense Layer Node Length Range 2 **Encoder**
Dense Layer Node Length Range **Prior Layer Length**
Reshape Layer **Tensor Shape Before Flattening**
Convolution Layer Kernel [1-2,10-25] Node Length Range 1-32 40% CO
Convolution Layer Kernel [1-2,10-25] Node Length Range 1-32 40% CO
Up Sampling Layer Kernel **Prior Pooling Kernel**
Convolution Layer Kernel [1-2,10-25] Node Length Range 1-32 40% CO
Convolution Layer Kernel [1-2,10-25] Node Length Range 1-32 40% CO
Up Sampling Layer Kernel **Prior Pooling Kernel**
Convolution Layer Kernel **Change in Current vs Input Shape** Node Length Range 1-32
Epoch Range 20-50
Batch Size 26-256
Model Trained on HS936 375000 cells/mL/ Microspheres 300000 cells/mL

Parabolic Extension

Extensions was run on signals and samples dimensions separately to avoid inaccuracy in wave restructuring.

1. Preliminary smoothing is done on raw signals. Windowed moving average
    a. 2 point window for samples/100 point window for signals
    b. Smoothed samples are squared
2. Each line is dissected separately and reconstructed.
    a. 3 data point arrays are selected, parabolas are fit.
    b. Maximum values are considered vertex's, slopes are averaged
    c. Parabolas are resampled at 100x original data length
3. Samples are overlapped starting at the 100^{th} data point of the previous sample
    a. Points are divided by the number of overlapping samples
4. Reconstructed matrices are smoothed after extension
    a. 200 point windowed moving average

Novel Feature AOV

Feature	sum_sq	df	F	PR
resolution_1_2_auc_signals:resolution_1_2_diff_signals	4.65E-10	1	8004.963	0
resolution_1_2_auc_signals:resolution_1_2_power_signals	1.45E-10	1	2505.71	0
resolution_1_2_auc_signals:resolution_1_4_auc_signals	4.14E-09	1	71397.07	0
resolution_1_2_auc_signals:resolution_1_4_power_signals	4.48E-08	1	771325.8	0
resolution_1_2_auc_signals:resolution_3_4_auc_signals	1.39E-10	1	2387.035	0
resolution_1_2_auc_signals:resolution_3_4_power_signals	3.10E-09	1	53355	0
resolution_1_2_diff_signals:resolution_1_2_power_samples	7.67E-09	1	132238.9	0
resolution_1_2_diff_signals:resolution_1_2_power_signals	1.70E-08	1	293675.2	0
resolution_1_2_diff_signals:resolution_1_4_auc_signals	8.10E-10	1	13963.02	0
resolution_1_2_diff_signals:resolution_1_4_diff_signals	1.78E-09	1	30716.34	0
resolution_1_2_diff_signals:resolution_1_4_power_samples	7.19E-08	1	1238460	0
resolution_1_2_diff_signals:resolution_1_4_power_signals	5.39E-08	1	928527.6	0
resolution_1_2_diff_signals:resolution_3_4_auc_signals	3.05E-09	1	52499.75	0
resolution_1_2_diff_signals:resolution_3_4_diff_signals	3.01E-09	1	51938.48	0
resolution_1_2_diff_signals:resolution_3_4_power_samples	2.85E-08	1	491143.1	0
resolution_1_2_diff_signals:resolution_3_4_power_signals	4.94E-07	1	8513252	0
resolution_1_2_power_samples:resolution_1_2_power_signals	2.45E-09	1	42257.89	0
resolution_1_2_power_samples:resolution_1_4_diff_signals	3.18E-09	1	54814.94	0
resolution_1_2_power_samples:resolution_1_4_power_signals	7.19E-09	1	123847.4	0
resolution_1_2_power_samples:resolution_3_4_auc_signals	2.13E-09	1	36764.61	0
resolution_1_2_power_samples:resolution_3_4_diff_signals	1.83E-10	1	3146.751	0
resolution_1_2_power_samples:resolution_3_4_power_signals	3.24E-09	1	55865.94	0
resolution_1_2_power_signals:resolution_1_4_auc_signals	2.05E-10	1	3527.075	0
resolution_1_2_power_signals:resolution_1_4_diff_signals	2.20E-07	1	3788220	0
resolution_1_2_power_signals:resolution_1_4_power_samples	1.49E-07	1	2574397	0

resolution_1_2_power_signals:resolution_1_4_power_signals	1.75E-08	1	302237.1	0
resolution_1_2_power_signals:resolution_3_4_auc_signals	1.93E-09	1	33338.41	0
resolution_1_2_power_signals:resolution_3_4_diff_signals	1.02E-08	1	174936.4	0
resolution_1_2_power_signals:resolution_3_4_power_samples	5.60E-09	1	96451.33	0
resolution_1_2_power_signals:resolution_3_4_power_signals	3.59E-08	1	617972	0
resolution_1_4_auc_signals:resolution_1_4_diff_signals	4.63E-10	1	7980.007	0
resolution_1_4_auc_signals:resolution_1_4_power_signals	4.95E-08	1	853722.3	0
resolution_1_4_auc_signals:resolution_3_4_diff_signals	4.29E-09	1	73850.32	0
resolution_1_4_auc_signals:resolution_3_4_power_signals	1.16E-09	1	20041.25	0
resolution_1_4_diff_signals:resolution_1_4_power_samples	7.65E-09	1	131908.5	0
resolution_1_4_diff_signals:resolution_1_4_power_signals	1.11E-08	1	190928.7	0
resolution_1_4_diff_signals:resolution_3_4_auc_signals	1.62E-10	1	2784.796	0
resolution_1_4_diff_signals:resolution_3_4_diff_signals	1.78E-08	1	306445.6	0
resolution_1_4_diff_signals:resolution_3_4_power_samples	9.83E-09	1	169431.1	0
resolution_1_4_diff_signals:resolution_3_4_power_signals	5.72E-08	1	986053.7	0
resolution_1_4_power_samples:resolution_1_4_power_signals	6.17E-09	1	106363.5	0
resolution_1_4_power_samples:resolution_3_4_auc_signals	4.87E-09	1	83980.53	0
resolution_1_4_power_samples:resolution_3_4_diff_signals	1.70E-10	1	2925.623	0
resolution_1_4_power_samples:resolution_3_4_power_signals	1.67E-09	1	28740.33	0
resolution_1_4_power_signals:resolution_3_4_auc_signals	1.51E-09	1	26031.48	0
resolution_1_4_power_signals:resolution_3_4_diff_signals	1.19E-07	1	2051975	0
resolution_1_4_power_signals:resolution_3_4_power_samples	1.58E-09	1	27163.18	0
resolution_1_4_power_signals:resolution_3_4_power_signals	1.28E-08	1	220467.3	0
resolution_3_4_auc_signals:resolution_3_4_power_samples	4.51E-09	1	77668.61	0
resolution_3_4_auc_signals:resolution_3_4_power_signals	1.07E-09	1	18361.21	0

resolution_3_4_diff_signals:resolution_3_4_power_samples	1.37E-10	1	2361.528	0
resolution_3_4_diff_signals:resolution_3_4_power_signals	3.07E-08	1	528784.8	0
resolution_3_4_power_samples:resolution_3_4_power_signals	2.08E-09	1	35758.98	0
resolution_1_4_auc_signals:resolution_1_4_power_samples	8.40E-11	1	1448.319	4.22E-247
resolution_1_4_auc_signals:resolution_3_4_power_samples	7.67E-11	1	1321.705	8.15E-230
resolution_1_2_auc_signals:resolution_1_4_diff_samples	6.50E-11	1	1120.005	5.30E-201
resolution_1_2_auc_signals:resolution_3_4_diff_signals	4.72E-11	1	813.216	8.95E-154
resolution_1_2_diff_signals:resolution_1_4_diff_samples	4.41E-11	1	759.9213	4.21E-145
resolution_1_2_auc_signals:resolution_1_2_diff_samples	3.95E-11	1	679.8489	8.72E-132
resolution_1_4_diff_samples:resolution_1_4_diff_signals	3.54E-11	1	610.1981	6.54E-120
resolution_1_2_auc_signals:resolution_3_4_diff_samples	3.04E-11	1	524.0231	8.04E-105
resolution_1_2_auc_signals:resolution_1_4_diff_signals	2.92E-11	1	503.2258	4.13E-101
resolution_1_2_auc_signals:resolution_1_2_power_samples	2.64E-11	1	455.386	1.80E-92
resolution_1_4_diff_samples:resolution_3_4_diff_signals	2.51E-11	1	432.1531	3.21E-88
resolution_1_2_auc_signals:resolution_3_4_power_samples	2.38E-11	1	409.4922	4.86E-84
resolution_1_2_diff_samples:resolution_1_2_diff_signals	2.37E-11	1	407.6002	1.09E-83

resolution_1_4_diff_samples:resolution_3_4_auc_signals	2.14E-11	1	368.102	2.59E-76
resolution_1_2_auc_signals:resolution_1_4_power_samples	2.05E-11	1	353.4106	1.53E-73
resolution_1_4_auc_signals:resolution_3_4_auc_signals	1.90E-11	1	327.0844	1.55E-68
resolution_1_2_diff_samples:resolution_1_4_diff_signals	1.85E-11	1	319.1012	5.24E-67
resolution_1_2_diff_samples:resolution_3_4_diff_signals	1.29E-11	1	221.6497	5.77E-48
resolution_1_2_diff_signals:resolution_3_4_diff_samples	8.31E-12	1	143.1973	4.50E-32
resolution_1_2_diff_samples:resolution_3_4_auc_signals	7.38E-12	1	127.2132	9.09E-29
resolution_1_4_diff_signals:resolution_3_4_diff_samples	6.84E-12	1	117.8289	8.14E-27
resolution_3_4_diff_samples:resolution_3_4_diff_signals	4.96E-12	1	85.4361	5.22E-20
resolution_3_4_auc_signals:resolution_3_4_diff_samples	4.47E-12	1	76.94107	3.32E-18
resolution_1_4_auc_signals:resolution_1_4_diff_samples	1.97E-12	1	33.87186	6.69E-09
resolution_3_4_auc_signals:resolution_3_4_diff_signals	1.37E-12	1	23.56005	1.29E-06
resolution_1_2_diff_samples:resolution_1_4_auc_signals	6.65E-13	1	11.46153	0.000722
resolution_1_2_power_signals:resolution_1_4_diff_samples	4.41E-13	1	7.591034	0.005911

[1] Sastre, J., M. L. Maestro, J. Puente, S. Veganzones, R. Alfonso, S. Rafael, J. A. Garcia-Saenz et al. "Circulating tumor cells in colorectal cancer: correlation with clinical and pathological variables." Annals of Oncology 19, no. 5 (2008): 935-938.
[2] Kurihara, Toshio, Takao Itoi, Atsushi Sofuni, Fumihide Itokawa, Takayoshi Tsuchiya, Shujirou Tsuji, Kentaro Ishii et al. "Detection of circulating tumor cells in patients with pancreatic cancer: a preliminary result." Journal of hepato-biliary-pancreatic surgery 15, no. 2 (2008): 189-195.
[3] Tanaka, Fumihiro, Kazue Yoneda, Nobuyuki Kondo, Masaki Hashimoto, Teruhisa Takuwa, Seiji Matsumoto, Yoshitomo Okumura et al. "Circulating tumor cell as a diagnostic marker in primary lung cancer." Clinical Cancer Research 15, no. 22 (2009): 6980-6986.
[4] Moreno, Jose G., S. Mark O'Hara, Steve Gross, Gerald Doyle, Herb Fritsche, Leonard G. Gomella, and Leon WMM Terstappen. "Changes in circulating carcinoma cells in patients with metastatic prostate cancer correlate with disease status." Urology 58, no. 3 (2001): 386-392.
[5] Hiraiwa, Kunihiko, Hiroya Takeuchi, Hirotoshi Hasegawa, Yoshiro Saikawa, Koichi Suda, Takashi Ando, Koshi Kumagai et al. "Clinical significance of circulating tumor cells in blood from patients with gastrointestinal cancers." Annals of Surgical Oncology 15, no. 11 (2008): 3092.
[6] Mitra, Abhisek, Lopa Mishra, and Shulin Li. "EMT, CTCs and CSCs in tumor relapse and drug-resistance." Oncotarget 6, no. 13 (2015): 10697.
[7] Abdallah, Emne Ali, Marcello Ferretti Fanelli, Virgílio Souza, e Silva, Marcelo Calil Machado Netto, Jose Luiz Gasparini Junior, Daniel Vilarim Araújo, Luciana Menezes Mendonça Ocea et al. "MRP1 expression in CTCs confers resistance to irinotecan-based chemotherapy in metastatic colorectal cancer." International journal of cancer 139, no. 4 (2016): 890-898.
[8] Gradilone, A., G. Naso, C. Raimondi, E. Cortesi, O. Gandini, B. Vincenzi, R. Saltarelli et al. "Circulating tumor cells (CTCs) in metastatic breast cancer (MBC): prognosis, drug resistance and phenotypic characterization." Annals of Oncology 22, no. 1 (2011): 86-92.
[9] Smerage, Jeffrey B., William E. Barlow, Gabriel N. Hortobagyi, Eric P. Winer, Brian Leyland-Jones, Gordan Srkalovic, Sheela Tejwani et al. "Circulating tumor cells and response to chemotherapy in metastatic breast cancer: SWOG S0500." Journal of Clinical Oncology 32, no. 31 (2014): 3483.
[10] Vitha, Mark F. Circulating tumor cells: isolation and analysis. John Wiley & Sons, 2016.
[11] Joosse, Simon A., and Klaus Pantel. "Biologic challenges in the detection of circulating tumor cells." Cancer research 73, no. 1 (2013): 8-11.
[12] Alunni-Fabbroni, Marianna, and Maria Teresa Sandri. "Circulating tumour cells in clinical practice: Methods of detection and possible characterization." Methods 50, no. 4 (2010): 289-297.
[13] Apostolaki, S., M. Perraki, A. Pallis, V. Bozionelou, S. Agelaki, P. Kanellou, A. Kotsakis et al. "Circulating HER2 mRNA-positive cells in the peripheral blood of patients with stage I and II breast cancer after the administration of adjuvant chemotherapy: evaluation of their clinical relevance." Annals of oncology 18, no. 5 (2007): 851-858.
[14] Scher, H. I., G. Heller, A. Molina, T. S. Kheoh, G. Attard, J. Moreira, S. K. Sandhu et al. "Evaluation of circulating tumor cell (CTC) enumeration as an efficacy response biomarker of overall survival (OS) in metastatic castration-resistant prostate cancer (mCRPC): Planned final analysis (FA) of COU-AA-301, a randomized, double-blind, placebo-controlled, phase III study of abiraterone acetate (AA) plus low-dose prednisone (P) post docetaxel." Journal of Clinical Oncology 29, no. 18_suppl (2011): LBA4517-LBA4517.
[15] Shapiro, Howard M. Practical flow cytometry. John Wiley & Sons, 2005.
[16] Andergassen, Ulrich, Alexandra C. Kölbl, Sven Mahner, and Udo Jeschke. "Real-time RT-PCR systems for CTC detection from blood samples of breast cancer and gynaecological tumour patients." *Oncology reports* 35, no. 4 (2016): 1905-1915.
[17] Beard, Paul. "Biomedical photoacoustic imaging." *Interface focus* 1, no. 4 (2011): 602-631.
[18] Galanzha, Ekaterina I., and Vladimir P. Zharov. "Photoacoustic flow cytometry." *Methods* 57, no. 3 (2012): 280-296.
[19] Haykin, Simon. *Neural networks: a comprehensive foundation*. Prentice Hall PTR, 1994.
[20] O'Brien, Christine M., Kyle D. Rood, Kiran Bhattacharyya, Thiago Q. DeSouza, Shramik Sengupta, Sagar K. Gupta, Jeffrey D. Mosley, Benjamin S. Goldschmidt, Nikhilesh Sharma, and John A. Viator. "Capture of

circulating tumor cells using photoacoustic flowmetry and two phase flow." *Journal of biomedical optics* 17, no. 6 (2012): 061221.

[21] Edgar, Robert H., Justin Cook, Cierra Noel, Austin Minard, Andrea Sajewski, Matthew Fitzpatrick, Rachel Fernandez, John D. Hempel, John A. Kellum, and John A. Viator. "Bacteriophage-mediated identification of bacteria using photoacoustic flow cytometry." *Journal of biomedical optics* 24, no. 11 (2019): 115003.

[22] Bankó, Petra, Sun Young Lee, Viola Nagygyörgy, Miklós Zrínyi, Chang Hoon Chae, Dong Hyu Cho, and András Telekes. "Technologies for circulating tumor cell separation from whole blood." *Journal of hematology & oncology* 12, no. 1 (2019): 48.

[23] Bankó, Petra, Sun Young Lee, Viola Nagygyörgy, Miklós Zrínyi, Chang Hoon Chae, Dong Hyu Cho, and András Telekes. "Technologies for circulating tumor cell separation from whole blood." *Journal of hematology & oncology* 12, no. 1 (2019): 48.

[24] Bankó, Petra, Sun Young Lee, Viola Nagygyörgy, Miklós Zrínyi, Chang Hoon Chae, Dong Hyu Cho, and András Telekes. "Technologies for circulating tumor cell separation from whole blood." *Journal of hematology & oncology* 12, no. 1 (2019): 48.

[25] Bankó, Petra, Sun Young Lee, Viola Nagygyörgy, Miklós Zrínyi, Chang Hoon Chae, Dong Hyu Cho, and András Telekes. "Technologies for circulating tumor cell separation from whole blood." *Journal of hematology & oncology* 12, no. 1 (2019): 48.

[26] Haykin, Simon. Neural networks: a comprehensive foundation. Prentice Hall PTR, 1994.

[27] Krizhevsky, Alex, Ilya Sutskever, and Geoffrey E. Hinton. "Imagenet classification with deep convolutional neural networks." In Advances in neural information processing systems, pp. 1097-1105. 2012.

[28] Galanzha, Ekaterina I., and Vladimir P. Zharov. "Circulating tumor cell detection and capture by photoacoustic flow cytometry in vivo and ex vivo." *Cancers* 5, no. 4 (2013): 1691-1738.

[29] He, Yun, Lidai Wang, Junhui Shi, Junjie Yao, Lei Li, Ruiying Zhang, Chih-Hsien Huang, Jun Zou, and Lihong V. Wang. "In vivo label-free photoacoustic flow cytography and on-the-spot laser killing of single circulating melanoma cells." *Scientific reports* 6 (2016): 39616.

[30] Gutierrez-Juarez, Gerardo, Sagar K. Gupta, Mays Al-Shaer, Luis Polo-Parada, Paul S. Dale, Chris Papageorgio, and John A. Viator. "Detection of melanoma cells in vitro using an optical detector of photoacoustic waves." *Lasers in Surgery and Medicine: The Official Journal of the American Society for Laser Medicine and Surgery* 42, no. 3 (2010): 274-281.

References

Abdallah, Emne Ali, Marcello Ferretti Fanelli, Virgílio Souza, e Silva, Marcelo Calil Machado Netto, Jose Luiz Gasparini Junior, Daniel Vilarim Araújo, Luciana Menezes Mendonça Ocea et al. "MRP1 Expression in CTCs Confers Resistance to Irinotecan-Based Chemotherapy in Metastatic Colorectal Cancer." *International Journal of Cancer* 139, no. 4 (2016): 890-898.

Alunni-Fabbroni, Marianna, and Maria Teresa Sandri. "Circulating Tumour Cells in Clinical Practice: Methods of Detection and Possible Characterization." *Methods* 50, no. 4 (2010): 289-297.

Andergassen, Ulrich, Alexandra C. Kölbl, Sven Mahner, and Udo Jeschke. "Real-time RT-PCR Systems for CTC Detection from Blood Samples of Breast Cancer and Gynaecological Tumour Patients." *Oncology Reports* 35, no. 4 (2016): 1905-1915.

Apostolaki, S., M. Perraki, A. Pallis, V. Bozionelou, S. Agelaki, P. Kanellou, A. Kotsakis et al. "Circulating HER2 mRNA-positive Cells in the Peripheral Blood of Patients with Stage I and II Breast Cancer After the Administration of Adjuvant Chemotherapy: Evaluation of Their Clinical Relevance." *Annals of Oncology* 18, no. 5 (2007): 851-858.

Bankó, Petra, Sun Young Lee, Viola Nagygyörgy, Miklós Zrínyi, Chang Hoon Chae, Dong Hyu Cho, and András Telekes. "Technologies for Circulating Tumor Cell Separation from Whole Blood." *Journal of Hematology & Oncology* 12, no. 1 (2019): 48.

Beard, Paul. "Biomedical Photoacoustic Imaging." *Interface Focus* 1, no. 4 (2011): 602-631.

Edgar, Robert H., Justin Cook, Cierra Noel, Austin Minard, Andrea Sajewski, Matthew Fitzpatrick, Rachel Fernandez, John D. Hempel, John A. Kellum, and John A. Viator. "Bacteriophage-mediated Identification of Bacteria Using Photoacoustic Flow Cytometry." *Journal of Biomedical Optics* 24, no. 11 (2019): 115003.

Galanzha, Ekaterina I., and Vladimir P. Zharov. "Circulating Tumor Cell Detection and Capture by Photoacoustic Flow Cytometry In Vivo and Ex Vivo." *Cancers* 5, no. 4 (2013): 1691-1738

Galanzha, Ekaterina I., and Vladimir P. Zharov. "Photoacoustic Flow Cytometry." *Methods* 57, no. 3 (2012): 280-296.

Gradilone, A., G. Naso, C. Raimondi, E. Cortesi, O. Gandini, B. Vincenzi, R. Saltarelli et al. "Circulating Tumor Cells (CTCs) in Metastatic Breast Cancer (MBC):

Prognosis, Drug Resistance and Phenotypic Characterization." *Annals of Oncology* 22, no. 1 (2011): 86-92.

Gutierrez-Juarez, Gerardo, Sagar K. Gupta, Mays Al-Shaer, Luis Polo-Parada, Paul S. Dale, Chris Papageorgio, and John A. Viator. "Detection of Melanoma Cells In Vitro Using an Optical Detector of Photoacoustic Waves." *Lasers in Surgery and Medicine: The Official Journal of the American Society for Laser Medicine and Surgery* 42, no. 3 (2010): 274-281.

Haykin, Simon. Neural Networks: A Comprehensive Foundation. Prentice Hall PTR, 1994.

He, Yun, Lidai Wang, Junhui Shi, Junjie Yao, Lei Li, Ruiying Zhang, Chih-Hsien Huang, Jun Zou, and Lihong V. Wang. "In Vivo Label-free Photoacoustic Flow Cytography and On-the-spot Laser Killing of Single Circulating Melanoma Cells." *Scientific Reports* 6 (2016): 39616.

Hiraiwa, Kunihiko, Hiroya Takeuchi, Hirotoshi Hasegawa, Yoshiro Saikawa, Koichi Suda, Takashi Ando, Koshi Kumagai et al. "Clinical Significance of Circulating Tumor Cells in Blood from Patients with Gastrointestinal Cancers." *Annals of Surgical Oncology* 15, no. 11 (2008): 3092.

Joosse, Simon A., and Klaus Pantel. "Biologic Challenges in the Detection of Circulating Tumor Cells." *Cancer Research* 73, no. 1 (2013): 8-11.

Krizhevsky, Alex, Ilya Sutskever, and Geoffrey E. Hinton. "Imagenet Classification with Deep Convolutional Neural Networks." *Advances in Neural Information Processing Systems*, pp. 1097-1105. 2012.

Kurihara, Toshio, Takao Itoi, Atsushi Sofuni, Fumihide Itokawa, Takayoshi Tsuchiya, Shujirou Tsuji, Kentaro Ishii et al. "Detection of Circulating Tumor Cells in Patients with Pancreatic Cancer: A Preliminary Result." *Journal of Hepato-Biliary-Pancreatic Surgery* 15, no. 2 (2008): 189-195.

Mitra, Abhisek, Lopa Mishra, and Shulin Li. "EMT, CTCs and CSCs in Tumor Relapse and Drug-Resistance." *Oncotarget* 6, no. 13 (2015): 10697.

Moreno, Jose G., S. Mark O'Hara, Steve Gross, Gerald Doyle, Herb Fritsche, Leonard G. Gomella, and Leon WMM Terstappen. "Changes in Circulating Carcinoma Cells in Patients with Metastatic Prostate Cancer Correlate with Disease Status." *Urology* 58, no. 3 (2001): 386-392.

O'Brien, Christine M., Kyle D. Rood, Kiran Bhattacharyya, Thiago Q. DeSouza, Shramik Sengupta, Sagar K. Gupta, Jeffrey D. Mosley, Benjamin S. Goldschmidt, Nikhilesh Sharma, and John A. Viator. "Capture of Circulating Tumor Cells

Using Photoacoustic Flowmetry and Two Phase Flow." *Journal of Biomedical Optics* 17, no. 6 (2012): 061221.

Sastre, J., M. L. Maestro, J. Puente, S. Veganzones, R. Alfonso, S. Rafael, J. A. Garcia-Saenz et al. "Circulating Tumor Cells in Colorectal Cancer: Correlation with Clinical and Pathological Variables." *Annals of Oncology* 19, no. 5 (2008): 935-938.

Scher, H. I., G. Heller, A. Molina, T. S. Kheoh, G. Attard, J. Moreira, S. K. Sandhu et al. "Evaluation of Circulating Tumor Cell (CTC) Enumeration as an Efficacy Response Biomarker of Overall Survival (OS) in Metastatic Castration-Resistant Prostate Cancer (mCRPC): Planned Final Analysis (FA) of COU-AA-301, a Randomized, Double-Blind, Placebo-Controlled, Phase III Study of Abiraterone Acetate (AA) Plus Low-Dose Prednisone (P) Post Docetaxel." *Journal of Clinical Oncology* 29, no. 18_suppl (2011): LBA4517-LBA4517.

Shapiro, Howard M. Practical Flow Cytometry. John Wiley & Sons, 2005.

Smerage, Jeffrey B., William E. Barlow, Gabriel N. Hortobagyi, Eric P. Winer, Brian Leyland-Jones, Gordan Srkalovic, Sheela Tejwani et al. "Circulating Tumor Cells and Response to Chemotherapy in Metastatic Breast Cancer: SWOG S0500." *Journal of Clinical Oncology* 32, no. 31 (2014): 3483.

Tanaka, Fumihiro, Kazue Yoneda, Nobuyuki Kondo, Masaki Hashimoto, Teruhisa Takuwa, Seiji Matsumoto, Yoshitomo Okumura et al. "Circulating Tumor Cell as a Diagnostic Marker in Primary Lung Cancer." *Clinical Cancer Research* 15, no. 22 (2009): 6980-6986.

Vitha, Mark F. Circulating Tumor Cells: Isolation and Analysis. John Wiley & Sons, 2016.